Generated using the official AMS LaTeX template v6.1

Entrainment, detrainment and dilution of dry and moist atmospheric thermals

Hugh Morrison

NSF National Center for Atmospheric Research, Boulder, CO USA

Corresponding author: Hugh Morrison, morrison@ucar.edu

ABSTRACT: This study examines entrainment, detrainment, and dilution of dry and moist (cloud) atmospheric thermals in large-eddy simulations. In a neutrally stable environment (with respect to dry dynamics), moist thermals have an increase in radius R with thermal height z_t ($\alpha \equiv dR/dz_t$) about 4 times smaller compared to dry thermals when density stratification is considered, and ~2.4 times smaller without density stratification (i.e., applying the Boussinesq approximation). An analytic expression relating α to several dimensionless parameters is derived from the thermal impulse-circulation relation to clarify the factors impacting α. This expression shows that the difference in buoyancy structure between moist and dry thermals, with buoyancy concentrated in the central cores of moist thermals owing to latent heating, explains their smaller spreading rates. Individual contributions of entrainment and detrainment are analyzed using a direct parcel-based approach in the simulations. Moist thermals have similar fractional detrainment but much smaller fractional entrainment rates compared to dry thermals, consistent with the differences in α. Despite having smaller α, moist thermals are similarly dilute (quantified by a passive tracer) as dry thermals because of their greater mixing efficiency with the environment. Thus, moist thermals are substantially dilute but expand much less in size/volume as they rise compared to dry thermals. α values for moist thermals in (dry) neutral and statically stable environments are similar, but fractional entrainment and especially detrainment rates are greater in the stable environment. Large detrainment rates are associated with a breakdown of the broader thermal vortex ring structure, especially with low environmental relative humidity, attributed in part to evaporation and buoyancy reversal.

SIGNIFICANCE STATEMENT: Thermals – blobs of rising buoyant air – are nearly ubiquitous in cumulus clouds. However, mechanisms by which cloud thermals mix with surrounding air and spread outward as they incorporate (entrain) this air are uncertain. Many past studies have examined dry thermals as a proxy for understanding cloud thermals. Using a numerical model, the current study shows that cloud thermals spread roughly 2-4 times less than dry thermals, but have a higher mixing efficiency. As a result, cloud thermals are similarly diluted by environmental air as dry thermals despite having a smaller spreading rate. This is important because dilution generally reduces the buoyancy of cloud thermals, helping to determine how fast and how far clouds as a whole rise.

1. Introduction

Several studies based on large-eddy simulations (LES) and observations showed that cumulus convection often comprises one or more rising thermal structures with a scale similar to the cloud width (e.g., Damiani et al. 2006; Sherwood et al. 2013; Romps and Charn 2015; Hernandez-Deckers and Sherwood 2016; Moser and Lasher-Trapp 2017; Peters et al. 2020). These thermals have a ring vortex-like structure with strong ascent near the center and descent along the periphery. Overall, entrainment and dilution of cumulus clouds appears to be closely linked to this flow structure. The thermals' toroidal circulations help to protect their central cores from entrainment and mixing with environmental air, and hence they are relatively undilute compared to other parts of clouds (Moser and Lasher-Trapp 2017; Morrison et al. 2020; Peters et al. 2020). In contrast, convergent flow near the thermal bottom is a region favored for intrusion of environmental air, with relatively high fractional entrainment rates as determined from LES (Moser and Lasher-Trapp 2017; Peters et al. 2020). Although these general features have been documented in previous studies, many details of entrainment, detrainment, and dilution in cumulus thermals remain poorly understood.

In contrast to cloud thermals, the dynamics of dry thermals are comparatively well known. If the thermal shape is self-similar – this is, that the thermal shape does not change over time – dimensional analysis shows that the spreading rate of thermal radius R with height of the thermal top z_t, $\alpha \equiv dR/dz_t$, is a constant[1] (note all symbols used in the paper are defined in Appendix C). This result has been confirmed by numerous laboratory and numerical modeling studies, with α

[1] A constant α following self-similarity and dimensional analysis is valid when there are no other physical length scales. This applies to dry thermals in an unstratified environment within an infinite domain.

of ~0.12-0.17 for thermals that are initially spherical and motionless (e.g., Scorer 1957; Escudier and Maxworthy 1973; Bond and Johari 2010; Zhao et al. 2013; Lai et al. 2015; Lecoanet and Jeevanjee 2019; Morrison et al. 2023). The primary mechanism for expansion of dry thermals is entrainment of environmental fluid by organized inflow from below the thermal (Zhao et al. 2013), with turbulent thermals entraining at a somewhat greater rate than in laminar flow (about 20-40% greater α as shown by Lecoanet and Jeevanjee (2019) and Morrison et al. (2022a)).

The net fractional entrainment rate ϵ_{net} of a thermal is defined as the relative increase in its mass M as it rises with height z_t (or decrease if $\epsilon_{net} < 0$): $\epsilon_{net} = M^{-1} dM/dz_t$. This is analogous to the standard definition of fractional entrainment (e.g., for plumes), except for thermals it is defined in a Lagrangian framework following the rising thermal top at height z_t rather than a fixed z relative to the ground. ϵ_{net} is the difference between the fractional entrainment and detrainment rates (where both are defined as positive quantities). Assuming that the thermal shape is self-similar and applying the Boussinesq approximation (constant density ρ in the equations of motion and mass continuity except for the buoyancy term), with a scaling relationship between R and thermal volume V given by $V = mR^3$ where m is a shape parameter, we may write

$$\epsilon_{net} = 3R^{-1}\alpha. \tag{1}$$

It follows that a dimensionless net entrainment efficiency can be defined as $e_{net} = \epsilon_{net} R$. From direct numerical simulation (DNS) of dry thermals, Lecoanet and Jeevanjee (2019, hereafter LJ2019) found that e_{net} is approximately constant after spin-up, implying that $\epsilon_{net} \propto R^{-1}$ consistent with dimensional analysis of self-similar thermals. They also showed that the detrainment of mass into the wake of dry thermals is small, implying $\epsilon_{net} \equiv \epsilon - \delta \approx \epsilon$, where ϵ and δ are the fractional entrainment and detrainment rates individually.

Given overall similarity of their vortex ring structures, it is tempting to assume that results for dry thermals should apply to the dynamics of moist thermals. However, latent heating and cooling (as well as the weight of condensate) in moist thermals drive different evolution of the buoyancy field. A few laboratory studies have examined thermals with an internal heating (buoyancy) source (Turner 1963; Kon and Magono 1976; Narasimha et al. 2011). These studies arrived at differing conclusions regarding the importance of latent heating on α, perhaps because of different experimental setups. Turner (1963) found that α was minimally smaller for thermals with increasing

buoyancy compared to those in a neutral environment (analogous to dry thermals), whereas Kon and Magono (1976) showed a large reduction in α for thermals with an internal heating source, and Narasimha et al. (2011) observed an initial increase in α when heating was first applied, followed by a substantial decrease. Morrison et al. (2021, hereafter MPS21) compared spreading rates of moist and dry thermals in axisymmetric simulations and found that moist thermals had a lower expansion rate, with α values about one-half those for dry thermals. They attributed this difference primarily to latent heating that led to increased buoyancy in the thermal inner core, thereby limiting thermal expansion. In contrast, Vybhav and Ravichandran (2022, hereafter VR22) found little difference in spreading rates between moist and dry turbulent thermals using DNS with a model applying simplified moist thermodynamics. Specific reasons for these differing results are unclear. Although MPS21 used a more detailed representation of moist thermodynamics using a microphysics scheme, a significant limitation was the use of an axisymmetric model. Another notable difference between these studies was that MPS21 included density stratification, while VR22 neglected density stratification following the Boussinesq approximation. Although the impacts of density stratification on dry thermals have been analyzed by Brandenburg (2016) and Anders et al. (2019), who proposed a $R \propto \rho^{-1/2}$ scaling, impacts of density stratification on moist versus dry thermals are unclear.

Another potentially important factor for thermal entrainment and mixing is the environmental static stability. Most studies have examined dry thermals in a neutrally stable environment, whereas atmospheric cumulus convection typically occurs in a (dry) statically stable environment. Besides directly impacting the rate of increase (or decrease) of thermal buoyancy, environmental static stability leads to gravity waves and can impact smaller-scale baroclinic instabilities and mixing (e.g., Grabowski 1993). It is also unclear if LJ2019's finding of negligible detrainment from dry thermals applies to moist thermals. VR22 found that thermal-environment mixing was enhanced for moist thermals, leading to a breakdown of the broader vortex ring structure and contributing to greater expansion of turbulent moist thermals compared to dry thermals. However, detailed analysis of entrainment and detrainment rates using a direct calculation (e.g., Yeo and Romps 2013) has yet to be performed for dry and moist thermals, to the knowledge of the author. Thus, understanding of entrainment and detrainment rates individually for dry and moist thermals is limited.

In the current study, building from the studies mentioned above, mechanisms of entrainment, detrainment, and dilution in dry and moist thermals are examined in detail. A theoretical expression is derived for α that depends on several dimensionless parameters corresponding to specific flow features. This expression also encapsulates the effects of density stratification on thermal spreading. Three-dimensional high-resolution numerical simulations (LES) of turbulent moist and dry thermals are analyzed to examine mechanisms of entrainment, detrainment, and dilution. Besides a focus on thermal spreading through net entrainment similar to MPS21 and VR22, entrainment and detrainment rates are analyzed individually using a direct parcel-based method similar to Yeo and Romps (2013), as well as thermal dilution via a passive tracer. Specific questions addressed are:

1) How do net entrainment and thermal spreading differ between moist and dry thermals, and what mechanisms explain the differences? How do these results compare to the axisymmetric simulations of MPS21 and the DNS of VR22?

2) What are differences in mixing and dilution between moist and dry thermals analyzed using a passive tracer and direct calculation of entrainment and detrainment rates?

3) How are answers to the above questions influenced by density stratification versus constant density approximation of the background fluid? How are entrainment, detrainment, and dilution of moist thermals impacted by environmental static stability?

This work is relevant to basic understanding of cumulus dynamics. Because cloud-scale thermals tend to contain relatively undilute air, an understanding of their behavior, particularly with regard to entrainment, detrainment and dilution, is crucial for understanding the ascent rates and terminal heights reached by clouds as a whole. This problem is therefore closely related to deep convection initiation and the deepening of an initially shallow cloud population. It is also relevant to convection parameterizations, particularly possible thermal-based parameterizations in the future.

The rest of the paper is organized as follows. Section 2 develops a theory for entrainment in dry and moist thermals, including an expression for α as a function of several dimensionless flow parameters. Section 3 describes the model and the modeling setup and analysis tools are detailed in section 4. Results from the model are presented in section 5. Section 6 provides a summary and highlights the main conclusions.

2. Theoretical background

a. Thermal spreading rate as a function of dimensionless parameters

A theoretical constraint on the spreading rate of thermal radius $\alpha \equiv dR/dz_t$ follows from the principle of momentum conservation via the impulse-circulation relation (e.g., Turner 1957; Lai et al. 2015; McKim et al. 2020); see Appendix A for details about this relation and its derivation. In the following, the impulse-circulation relation is non-dimensionalized and used to derive an expression for α as a function of several dimensionless flow parameters. This allows for a more thorough understanding of how various flow features and parameters impact α when analyzing the numerical simulations presented later. For simplicity, we first apply the incompressible Boussinesq approximation (meaning constant $\rho = \rho_0$); the case for a density-stratified environment with $\rho = \rho(z)$ is discussed later. We apply the Boussinesq approximation to the impulse-circulation equation (eq A6 in Appendix A) and combine it with the expression for volume-integrated buoyant forcing of a spheroidal thermal $F_b = \rho_0 \frac{4}{3}\pi R^2 H B_t$, where R is the thermal radius, H is the vertical half-depth of the thermal (vertical depth divided by 2), and B_t is the thermal volume-averaged buoyancy.. This gives

$$2\zeta^2 \Gamma w_t \alpha = \frac{4}{3} R H B_t - \zeta^2 R \int_{z_b}^{z_t} B_c dz \tag{2}$$

where Γ is the thermal's circulation, ζ is a dimensionless length parameter equal to the ratio of the vortex core radius R_{vc} to thermal radius R (see Appendix A), w_t is the thermal's ascent rate, and the difference between the thermal top and bottom heights is $z_t - z_b = 2H$. A dimensionless parameter $\sigma \equiv (2HB_t)^{-1} \int_{z_b}^{z_t} B_c dz$ is introduced that is defined solely in terms of the spatial distribution of buoyancy within the thermal, where B_c is buoyancy along the thermal's central vertical axis. Small values of buoyancy along the thermal's vertical axis relative to the thermal-mean B_t imply small values of σ. For the dry case, $\sigma \approx 0$ since there is little buoyancy along the vertical axis after spinup (McKim et al. 2020; Morrison et al. 2021). For moist thermals with substantial latent heating along the vertical axis, it is expected $\sigma \approx 1$ or somewhat greater which is demonstrated by numerical simulations later.

Using parameter σ in (2) and rearranging terms gives

$$\zeta^2 \Gamma w_t \alpha = R H B_t \left(\frac{2}{3} - \sigma \zeta^2 \right). \tag{3}$$

The right-hand-side represents a buoyant acceleration generalized for any buoyancy distribution via σ. All else equal, (3) implies that α should be larger for dry compared to moist thermals if dry thermals have smaller σ. However, the buoyancy and velocity magnitudes may generally be quite different for moist and dry thermals. Thus, the response of α to latent heating in moist thermals is not obvious from (3). We re-cast the impulse-circulation equation in a non-dimensional form to gain further insight.

First, we turn to the Boussinesq thermal vertical momentum budget to relate w_t to B_t. In a simple form, this can be expressed as Morrison et al. (2022a, 2023)

$$\frac{1}{2}\frac{dw_t^2}{dz_t} = B_t + F_e + F_p \tag{4}$$

where F_e is the vertical momentum entrainment and F_p is a pressure acceleration term that includes buoyant and dynamic perturbation pressure contributions. Entrainment and perturbation pressure contribute to an effective downward acceleration and decrease w_t, while B_t contributes to upward acceleration when > 0 or downward acceleration when < 0. For dry thermals, entrainment can be expressed in terms of α and the pressure acceleration term by dimensionless drag coefficient and virtual mass parameters in (4) to derive an analytic expression for dw_t/dz (Eq. 8 in Morrison et al. 2023). However, latent heating and cooling from condensation and evaporation in moist thermals add considerable complexity. Therefore, here it is simply assumed that the acceleration terms F_e and F_p are proportional to B_t following dimensional consistency, and encapsulate their net influence via a dimensionless parameter c_f that is defined by how efficiently buoyant acceleration is converted to vertical momentum. This is expressed as

$$\frac{1}{2}\frac{dw_t^2}{dz_t} \approx c_f B_t. \tag{5}$$

We solve for w_t by integrating (5) from the initial thermal top height to height z_t as the thermal rises over time. To do so, another dimensionless parameter c is introduced which is defined by $c \equiv \int_0^{z_t} c_f B_t(z')dz'/(z_t B_t(z_t))$, where z' is a dummy variable of integration following the thermal top[2]. In effect, c^{-1} is a Froude number (ratio of inertia to effective buoyant forcing) that depends on the shape of the $c_f B_t$ profile as the thermal rises over time. For example, a linear increase of

[2]For simplicity, a vertical coordinate is chosen such that the initial thermal top height is at $z = 0$.

B_t with zero initial buoyancy and constant c_f has $c = c_f/2$. Integrating (5) from $z' = 0$ to $z' = z_t$, using the definition of c, and rearranging terms gives an expression for w_t:

$$w_t = \sqrt{2cB_t z_t}. \tag{6}$$

Next, following dimensional consistency, a dimensionless circulation parameter $b \equiv \Gamma/(Rw_t)$ is introduced. Using this definition in (3), combining the resulting expression with (6), and rearranging terms gives

$$z_t \alpha = \frac{H}{2bc\zeta^2}\left(\frac{2}{3} - \sigma\zeta^2\right). \tag{7}$$

Finally, we divide (7) by z_t and introduce a dimensionless parameter $f \equiv H/z_t$, which is defined by how the thermal's vertical length varies with height as it rises. This gives an expression for α as a function of the four dimensionless flow parameters b, c, f, and ζ, as well as the dimensionless buoyancy parameter σ, valid for the Boussinesq approximation:

$$\alpha = \frac{f}{2bc\zeta^2}\left(\frac{2}{3} - \sigma\zeta^2\right). \tag{8}$$

Note that only two parameters are needed to fully describe α for the Boussinesq case using (8), since $f/(bc\zeta^2)$ and $\sigma\zeta^2$ may be consolidated into two dimensionless parameters. However, we keep the five parameters separate here to facilitate physical interpretation of the numerical simulations.

The numerical results in section 5 show that, with the exception of σ, the dimensionless parameters are similar overall between moist and dry thermals and fairly constant beyond spin up (i.e., once the thermal's toroidal circulation becomes well established). This indicates a universality of the general flow structure of moist and dry thermals and the relationships between forcing, vertical velocity, and circulation. That said, the initial thermal shape (shape of the initial buoyancy perturbation) is expected to impact the dimensionless parameters and hence α following (8). The impact of initial thermal shape on entrainment behavior has been documented previously for dry thermals (e.g., Lai et al. 2015; Morrison et al. 2023), but is not examined in the current study. As will be shown in section 5, differences in the buoyancy distribution between moist and dry thermals, encapsulated by σ, explain slower spreading rate of moist compared to dry thermals. Physically, this occurs because the impact of different spatial distributions of buoyancy on baroclinic generation

and destruction of vorticity leading to a rapid outward spread of the vorticity maximum for dry thermals but lesser spread for moist thermals.

b. Effects of density stratification

Brandenburg (2016) and Anders et al. (2019) examined the case of horizontal compression of descending thermals in a density-stratified environment. Combining (A4) with $I_z = F_b$ (A5) from Appendix A, where I_z is the impulse in the z direction (height), assuming constant F_b valid for dry thermals after spin up in a neutrally stable environment with no sources or sinks of buoyancy, indicates a dependence of R on $\rho_t^{-1/2}$. For "pure" compression or expansion, in which the thermal shrinks or grows solely from density stratification, R only changes in response to $\rho(z)$, and thus $R \propto \rho_t^{-1/2}$ (Brandenburg 2016). To generalize for moist thermals, in which F_b cannot be assumed constant after spinup, here we take a different approach and instead generalize (8) to include the effects of density stratification.

Assuming $\rho = \rho(z)$ and neglecting horizontal density variations owing to compressibility, we combine (A6) with the same set of dimensionless parameters defined above for the Boussinesq case. This gives, after rearranging terms,

$$2\zeta^2 bcz_t\alpha = H\left(\frac{2}{3} - \sigma\zeta^2\right) - bc\zeta^2 Rz_t\frac{d\ln\rho_t}{dz_t}. \tag{9}$$

An additional dimensionless parameter is introduced that is defined by the thermal's aspect ratio: $h \equiv R/H$. Combining this with (9), dividing by z_t, and rearranging terms gives our final expression for the thermal expansion rate that includes effects of density stratification:

$$\alpha = \frac{f}{2bc\zeta^2}\left(\frac{2}{3} - \sigma\zeta^2 - bc\zeta^2 hz_t\frac{d\ln\rho_t}{dz_t}\right). \tag{10}$$

For thermals with a self-similar shape, h is constant with height. In contrast, the magnitude of $z_t d\ln\rho_t/dz_t$ tends to increase with height for typical atmospheric density profiles. Since the other dimensionless parameters are also quasi-constant with height, and $d\ln\rho_t/dz < 0$, this implies an increase of α with height in a density stratified environment. For a typical atmospheric density profile, the magnitude of $z_t d\ln\rho_t/dz_t$ increases by about a factor of 4 between 3 and 10 km altitude. This increase of α with height is qualitatively consistent with the $R \propto \rho_t^{-1/2}$ scaling for

rising thermals under "pure" expansion applied to a typical atmospheric density profile (where $dR/dz_t \propto d\rho_t^{-1/2}/dz_t \propto -\rho_t^{-3/2} d\rho_t/dz_t$).

3. Model description

The Cloud Model 1 (CM1, Bryan and Fritsch 2002) version r21.0 is used for all numerical simulations in this study. CM1 is a non-hydrostatic model primarily used to simulate atmospheric flows. Most of the simulations use an isotropic grid spacing of 75 m, but an additional smaller set of simulations use a grid spacing of 32.5 m to examine robustness of the main results to increasing grid resolution (see Appendix B). Advection is based on a fifth-order Weighted Essentially Non-Oscillatory (WENO) scheme (Jiang and Shu 1996). The model physical domain size is 12×12 km^2 horizontally and 16 km vertically for all simulations. Simulations are run until the thermal top reaches between 9 and 10 km, or 30 min (whichever comes first). The adaptive time step option in CM1 is employed. The model setup uses periodic lateral boundary conditions with the top and bottom boundaries rigid and free slip.

Several sets of experiments are performed to examine how thermal entrainment, detrainment, and dilution are influenced by: 1) dry versus moist thermal dynamics, 2) density stratified versus unstratified environments, and 3) neutrally stable versus statically stable environments. To examine dry versus moist dynamics, one could use an environment that is neutrally stable with respect to dry dynamics for the dry thermal simulations and neutrally stable to moist dynamics for the moist thermal simulations (e.g., Bryan and Fritsch 2002). However, because conditions are generally cloud-free in the environment outside of moist thermals, flow outside of the thermals will be statically stable; such a setup would therefore confound impacts of static stability and dry versus moist dynamics. Instead, both dry and moist thermal simulations are run here with an environmental profile that is neutrally stable to dry dynamics (hereafter "dry-neutral"). A dry-neutral profile removes complications from gravity waves and wave drag and also allows dry thermals (with no buoyancy source or sink) to rise a significant height. An additional set of moist thermal simulations apply a (dry) statically stable environment to examine the impacts of static stability, detailed below. All simulations are initially motionless and exclude environmental wind shear.

Simulations with the dry-neutral environment (for dry and moist thermals) use a constant environmental potential temperature θ of 300 K. In these conditions, a dry-neutral environment

will produce large buoyancy and vertical velocity as moist thermals rise above the level of free convection. To examine the impact of buoyancy and velocity scales, an additional set of moist thermal simulations with the dry-neutral environment reduce the latent heating by a factor of 2, which produces much smaller w_t. To enforce consistency between the water vapor mixing ratio q_v, temperature T, and pressure p in these reduced heating simulations, similar to MPS2021, q_v is re-diagnosed from T and p to retain exactly saturated conditions each time step after scaling the latent heating increment and adding it to T. The difference before and after re-diagnosing q_v is used to calculate the change in cloud water during the time step. In effect, this modification increases the moist adiabatic lapse rate within cloud so that it is closer to dry adiabatic. Evaporation is unmodified in this case.

The case with a statically stable environment for moist thermals applies the analytic temperature profile from Weisman and Klemp (1982, hereafter WK), which represents an idealized profile typical of mid-latitudes with moderate lapse rates in the lower to middle troposphere. No adjustments to latent heating are made in the WK simulations.

The water vapor profile in both the dry-neutral and WK moist thermal simulations is the same, and is based on the Weisman and Klemp (1982) profile below 1.5 km (with a low level q_v of 14 g kg^{-1}) and a constant relative humidity (RH) of either 85 or 42.5% above 1.5 km. As will be shown, free tropospheric RH has a large impact on entrainment, detrainment, and dilution in the statically stable environment. The level of free convection in the moist simulations is at about 1.1 km in both the dry-neutral and WK cases.

To examine the impacts of density stratification, this study employs both the compressible and incompressible Boussinesq dynamical solver options in CM1. Density stratification is considered in the former and a constant background density in the latter. The compressible option employs split time steps with sub-stepping for acoustic modes treated using a vertically implicit and horizontally explicit approach. The Boussinesq solver uses the incompressible mass continuity equation with pressure retrieved diagnostically. The dry and moist thermal simulations with a dry-neutral environment are compared both with and without density stratification. The moist thermal simulations with the stably stratified WK environment apply only the density stratified environment using the compressible solver.

The microphysics is simplified to avoid complications from precipitation and cold pools. The moist simulations use the Morrison et al. (2009) bulk scheme but with cloud water condensation and evaporation (calculated via the saturation adjustment) as the only processes considered. Cloud water is included in the buoyancy calculation while impacts of vapor on buoyancy are neglected so that the environmental static stability is identical between the moist and dry simulations. Subgrid-scale mixing is based on a Smagorinsky-type approach that includes modifications to account for stable stratification (Stevens et al. 1999, Appenbdix B section b therein). All other physical processes (e.g., radiation) are neglected for simplicity.

Thermals are initiated by adding a spherical bubble of buoyant air with a 2 K θ perturbation to the initial conditions. Although the velocity scale changes as expected, there is little sensitivity of dry thermal entrainment, detrainment and dilution to changes in the initial θ of the bubble (see section 5a). The initial bubble radius in all cases is 750 m; so the thermals are initially 20 grid points across in the 75 m grid spacing simulations and hence well resolved. The thermals are initially placed at a height of 750 m; thus, their buoyancy anomaly extends to the surface. This is meant to represent convective thermals originating in the lower troposphere. A nearby surface boundary can impact the effective buoyant forcing (Jeevanjee and Romps 2016), but the thermal spreading rate α is nearly the same in the simulations here compared to those of (Morrison et al. 2023), who initialized thermals at a distance of 4 radii from the lower boundary. Further investigating the impact of initial thermal height relative to the surface is beyond the scope of this study. Smaller amplitude grid-scale random perturbations ($\pm$0.5 K) are applied to the initial θ within the bubble to break axisymmetry and generate turbulent-like flow.

A list of the main simulations is given in Table 1. The naming of simulations is as follows: dry (DRY) versus moist (MOIST) and Boussinesq (B) versus compressible (C). For moist simulations, there is an additional designation for the dry-neutral environmental profile with no latent heating adjustment (LH1.0) or with latent heating reduced by a factor of 2 (LH0.5), or the statically-stable profile based on the Weisman-Klemp sounding (WK). Configurations of the moist WK runs use either 42.5 or 85% free tropospheric relative humidity (RH), which is included as another naming designation, and compressible dynamics (note that "MOIST" and "C" are excluded in the names since the WK simulations are only run with moist and compressible dynamics). The moist runs with the dry-neutral environment set the free tropospheric RH to 85%.

TABLE 1. Description of the main set of LES ensembles. Compressible simulations have a density-stratified environment whereas Boussinesq simulations assume constant density of the background fluid except for the buoyancy term in the vertical momentum equation.

Name	Dynamical solver	Background static stability	Latent heat scaling	Free tropospheric RH
DRY-C	Compressible	Dry-neutral	N/A	N/A
DRY-B	Boussinesq	Dry-neutral	N/A	N/A
MOIST-C-LH0.5	Compressible	Dry-neutral	0.5	85%
MOIST-C-LH1.0	Compressible	Dry-neutral	1.0	85%
MOIST-B-LH0.5	Boussinesq	Dry-neutral	0.5	85%
MOIST-B-LH1.0	Boussinesq	Dry-neutral	1.0	85%
WK-RH0.425	Compressible	Weisman-Klemp	1.0	42.5%
WK-RH0.85	Compressible	Weisman-Klemp	1.0	85%

4. Experimental design and analysis methodology

Given the nonlinear dynamics of the turbulent flow, small changes to the initial conditions lead to spread in model results. Thus, a 5-member ensemble is run for each configuration listed in Table 1 to improve robustness. Different ensemble members are generated using different random number seeds for the small-amplitude θ perturbations within the initial bubble.

a. Thermal tracking procedure

In order to analyze the thermals' behavior as they evolve, thermal boundaries must be determined and tracked. An objective thermal tracking method is employed similar to Romps and Charn (2015), LJ2019, and Morrison et al. (2022a, 2023). The thermal horizontal center x_c is obtained by finding the column with maximum vertically-integrated dynamic perturbation pressure. Given relative smoothness of the pressure field, this was found to be superior to using the vertical velocity or other fields to define x_c. In the next step, the model fields are re-gridded from the native Cartesian coordinates to axisymmetric coordinates (r, z) centered on x_c. The thermal top velocity W is found by the ascent rate of the thermal top defined by the buoyancy field similarly to LJ2019. W

is subtracted from the w field. Streamlines are then obtain by integrating

$$\frac{\partial \psi}{\partial r} = 2\pi r \left(w_{axi} - W \right), \tag{11}$$

$$\frac{\partial \psi}{\partial z} = -2\pi r u_{axi}, \tag{12}$$

where u_{axi} and w_{axi} are the re-gridded, azimuthally-averaged radial and vertical velocities in axisymmetric cylindrical coordinates with the boundary condition $\psi\left(r = 0, z = z_t\right) = 0$. The thermal boundary is defined by the $\psi = 0$ isoline, which passes through the thermal top by construction. The thermal volume encompasses the region with $\psi > 0$. Thermal radius R is defined as the widest region horizontally (considering all vertical levels) with $\psi > 0$. Note that some previous studies (LJ2019; Morrison et al. 2022) employed an additional step to reduce noise in W from the discretization. This was done by fitting data to the analytic scaling for dry thermals ($W \propto t^{-1/2}$) based on similarity theory. Because this is applicable to dry thermals but not moist, this extra step is not used here. While individual simulations have some noise in W and hence R and other thermal properties, the impact of this noise is reduced by the ensemble approach. Overall, the thermal tracking method works well in identifying thermal boundaries subjectively by visual inspection of plots, and objectively by the close comparison between W and the thermal volume-averaged w (w_t) (Fig. 1a). The difference in W and w_t in terms of mean error and mean absolute error is 3.3% (w_t is always slightly smaller than W).

b. Parcel-based direct entrainment and detrainment

A parcel-based method is used to calculate entrainment and detrainment rates directly similar to Yeo and Romps (2013), Tian and Kuang (2016), Kirshbaum (2020), and others. For this method, the built-in parcel tracking in CM1 is utilized. Parcels are initialized at the start of each simulation, placed in the center of each grid cell below 12 km and horizontally within the inner 7 km of the domain, giving 1,444,000 total parcels. Each parcel represents the total mass of air in a grid cell that accounts for the change in ρ with height in the density stratified simulations. The total entrainment rate E (units of kg/s) is calculated at each analysis step as the sum of the mass of all parcels that are within the thermal volume (defined by the thermal boundaries determined using the tracking method detailed above) at that step but were outside of the thermal at the previous step,

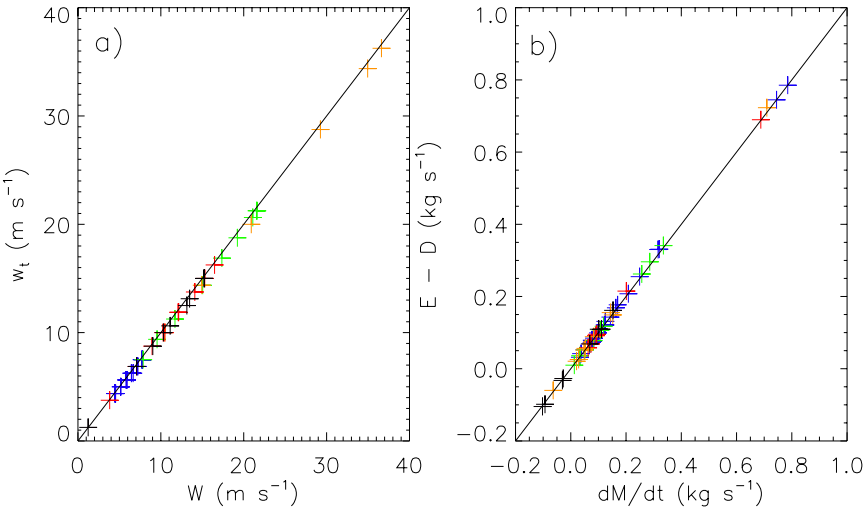

FIG. 1. a) Comparison of thermal top ascent rate W with the thermal volume-averaged vertical velocity w_t. b) Comparison of the net entrainment $E - D$ (total change in thermal mass per time) from the parcel calculation with the change in total thermal mass with time dM/dt calculated independently from the thermal tracking algorithm. In both plots, results are shown at 1 min intervals for single ensemble members of DRY-C (blue), MOIST-C-LH0.5 (green), MOIST-C-LH1.0 (red), WK-RH0.85 (orange), and WK-RH0.425 (black). The black diagonal lines show a 1:1 relationship.

divided by the length of the analysis step (60 sec). Total detrainment D (same units as E) is defined similarly except that it is the sum of all parcel masses that were located inside of the thermal at the previous step and at the current step are outside of the thermal. Fractional rates of entrainment ϵ and detrainment δ (units of m^{-1}) are calculated as $\epsilon = E/(\rho w_t V)$ and $\delta = D/(\rho w_t V)$. Entrainment e and detrainment d efficiencies (unitless) are calculated as $e = \epsilon R$ and $d = \delta R$. The calculations are analogous to traditional definitions of these quantities but integrated vertically to account for mass exchange through the depth of the thermal. Thus, fractional entrainment, for example, is defined here as the relative increase in total thermal mass from entrainment per unit length as the thermal rises. Note that 60 sec is somewhat longer for the time discretization than some previous studies of direct entrainment/detrainment using parcels (e.g., 30 sec in Kirshbaum et al. 2023). In general, it is expected that entrainment/detrainment rates will increase with higher time resolution or more parcels to provide better spatial resolution. Indeed, tests with a 30 sec discretization and parcel density increased by a factor of 2^3 (i.e., distance between parcels reduced by a factor of 2 in each direction) give an increase in E and D by 7-28% and 31-66%, respectively, as expected.

However, differences between moist and dry simulations are consistent and net entrainment ($E-D$) decreases only slightly (by 4-10%).

To further test robustness of this approach, we compare the change in mass of the thermals as they rise, calculated directly from the thermal volume and air density, and the change in thermal mass calculated as $E-D$ following the parcel calculations. Fig. 1b shows a close comparison of the two, with the $E-D$ calculation lying close to the 1:1 line. Overall, error is small with with mean error of 1.1% and mean absolute error of 4.1%.

c. Passive tracer

To analyze dilution, a passive tracer is added to the initial conditions that is set to 1 kg kg^{-1} within the bubble and 0 kg kg^{-1} elsewhere. Tracer values less than 1 kg kg^{-1} within the thermal as it evolves indicate dilution of thermal air. LJ2019 also used a passive tracer (identical to the perturbation density in their Boussinesq simualtions with no sources or sinks of buoyancy) to analyze net detrainment from the thermal. They quantified this as the fraction of total tracer mass below the thermal (below the level of the lowest point in the thermal). This measure of net detrainment is also analyzed here.

5. Results

a. Basic results for the Boussinesq case

Figure 2 presents vertical cross sections in the $X-Z$ plane through the thermal center of the buoyancy and vertical velocity fields for members of the DRY-B and MOIST-B-LH0.5 ensembles (Boussinesq with the dry-neutral environment) at three different times as the thermals rise. MOIST-B-LH1.0 (not shown) gives similar overall behavior to MOIST-B-LH0.5. All of the dry and moist thermals contain ring-vortex-like circulations with strong ascent in the center and descent along their periphery. Both the DRY-B and MOIST-B-LH0.5 thermals expand as they rise, which is evident from the thermal boundaries (thick black lines in Fig. 2). However, it is clear that, for the same height of the thermal top, the thermal in DRY-B expands horizontally much more than in MOIST-B-0.5. For example, at a thermal top height z_t ~8 km, the DRY-B thermal radius is about 1.7 times larger than that in MOIST-B-0.5. On the other hand, the MOIST-B-0.5 thermal expands more vertically. However, as detailed later, volume expansion is greater in DRY-B than MOIST-

LH-0.5, with ensemble mean V about a factor of 2 greater in DRY-B at z_t ~8 km. Note that the region of downward motion in Fig. 2 appears to widen substantially over time for MOIST-B-LH0.5, with a greater width than in DRY-B after heights of the thermals' tops reach 5-6 km. However, this occurs because the same contour lines for w are used for DRY-B and MOIST-B-LH0.5 in Fig. 2. If the w contours were instead scaled by the thermals' overall vertical velocity, which is a factor of 2-3 greater for MOIST-B-LH0.5 than DRY-B, then the width of the region of downward motion would be fairly constant in time for MOIST-B-LH0.5 and similar to DRY-B overall.

Another obvious difference between the DRY-B and MOIST-B-LH0.5 thermals is the difference in buoyancy. Not only is the magnitude of buoyancy much greater in MOIST-B-LH0.5, but large values of buoyancy are concentrated in the thermal's core along its vertical axis. There is also a narrow stem of positive buoyancy trailing the thermal, and some regions of negative buoyancy mainly in the thermal wake associated with evaporation and latent cooling. In contrast, with no sources or sinks of buoyancy in DRY-B, the largest values of buoyancy are concentrated around the center of rotation in the ring-like vortex surrounding the core. This feature of dry buoyant thermals has been documented in several previous studies (e.g., Lai et al. 2015; LJ2019; MPS21; VR22; Morrison et al. 2023).

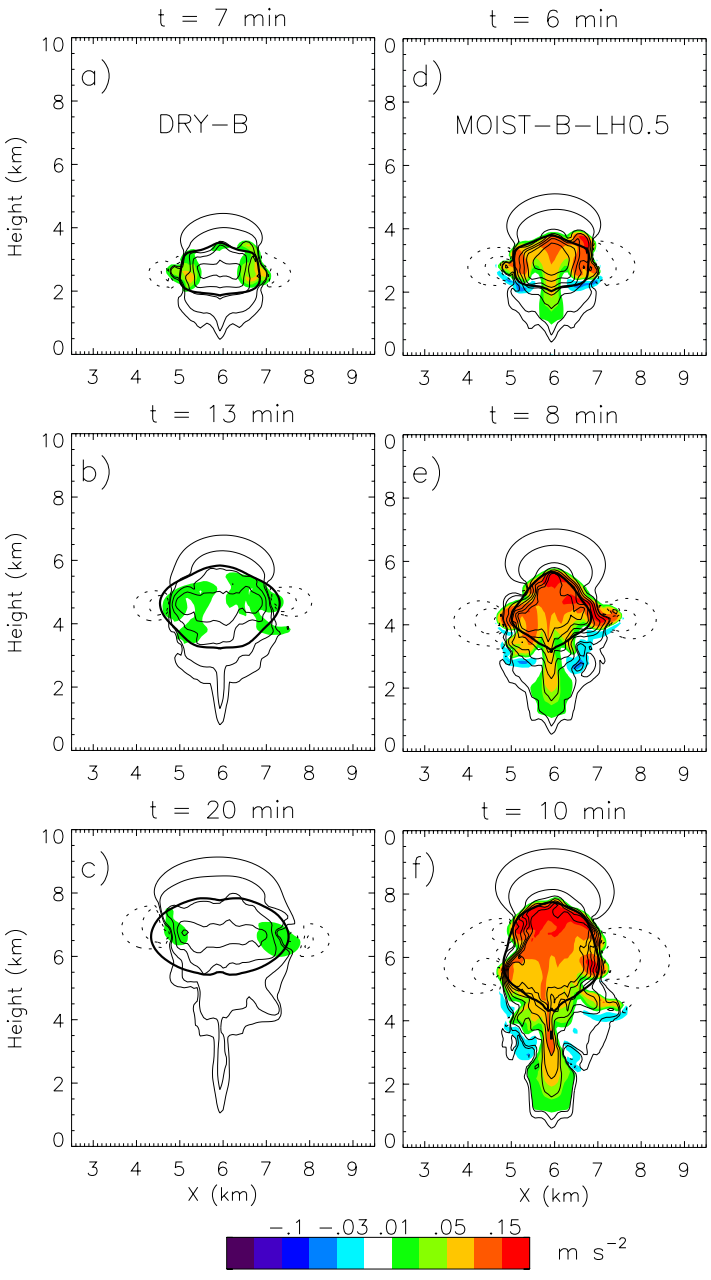

FIG. 2. Vertical cross sections through the thermal center of buoyancy (color contours) and vertical velocity w (black contour lines) at different times as indicated for single members of the a, b, c) DRY-B and d, e, f) MOIST-B-LH0.5 ensembles. Thick black lines indicate the thermal boundaries. The contour intervals for w are 1, 2, and thereafter every 4 m s^{-1} indicated by solid thin black lines, with the same contours for negative w shown by dotted lines.

The evolution of various properties as the thermals rise is quantified in Fig. 3. This figure shows thermal radius R, volume V, ascent rate w_t, and mean buoyancy B_t as a function of thermal top height z_t for the DRY-B, MOIST-B-LH0.5, and MOIST-B-LH1.0 ensembles. Results for individual ensemble members as well as the ensemble means are presented. Spreading of thermals is seen by the increase of R and V with z_t. Ensemble means and standard deviations of α calculated directly from dR/dz_t and averaged for z_t between 3 and 10 km are shown in Table 2. While there is considerable spread among members of each ensemble, it is clear that the DRY-B thermals have a much greater expansion rate than the moist thermals. There are no significant differences in R and V between the MOIST-B-LH0.5 and MOIST-B-LH1.0 ensembles, indicating that the magnitude of latent heating is unimportant as long as it is large enough to produce buoyancy along the thermal's vertical axis greater than the initial B perturbation. This aspect is discussed more below. An additional set of moist thermal simulations with environmental RH (above 1.5 km) set to 42.5% give similar overall results to the main set of simulations with RH of 85% for the dry-neutral environment (not shown). While there is some decrease in ensemble mean R and V for thermals in the dry-neutral environment with the reduction in environmental RH, the differences are well within the ensemble spreads and therefore may not be robust. This relative insensitivity to environmental RH in the dry-neutral environment contrasts with thermals in the WK environment discussed later.

With substantial differences in latent heating (which is absent in DRY-B), B_t and w_t are considerably different among the ensembles (Fig. 3c,d). The DRY-B thermals have a characteristic decrease in B_t which scales with V^{-1} as thermal buoyancy is diluted by environmental air while the thermal entrains and expands. The moist thermals also entrain environmental air, but B_t is nearly constant with z_t for MOIST-B-LH-0.5 with the source of buoyancy from latent heating. With greater latent heating in MOIST-B-LH1.0, the ensemble-mean B_t increases with z_t below 7 km. Above this height, B_t decreases as latent heating weakens at lower temperatures while the thermals continue entraining. Similar trends are seen for w_t. In DRY-B, there is an initial increase of w_t as the thermals' circulations spin up, and it decreases above ~3 km primarily due to loss of w momentum from entrainment and the reduction of B_t. This reduction of w_t for the dry thermals scales approximately with z_t^{-1} in accordance with theory (Tarshish et al. 2018; Morrison et al. 2023).

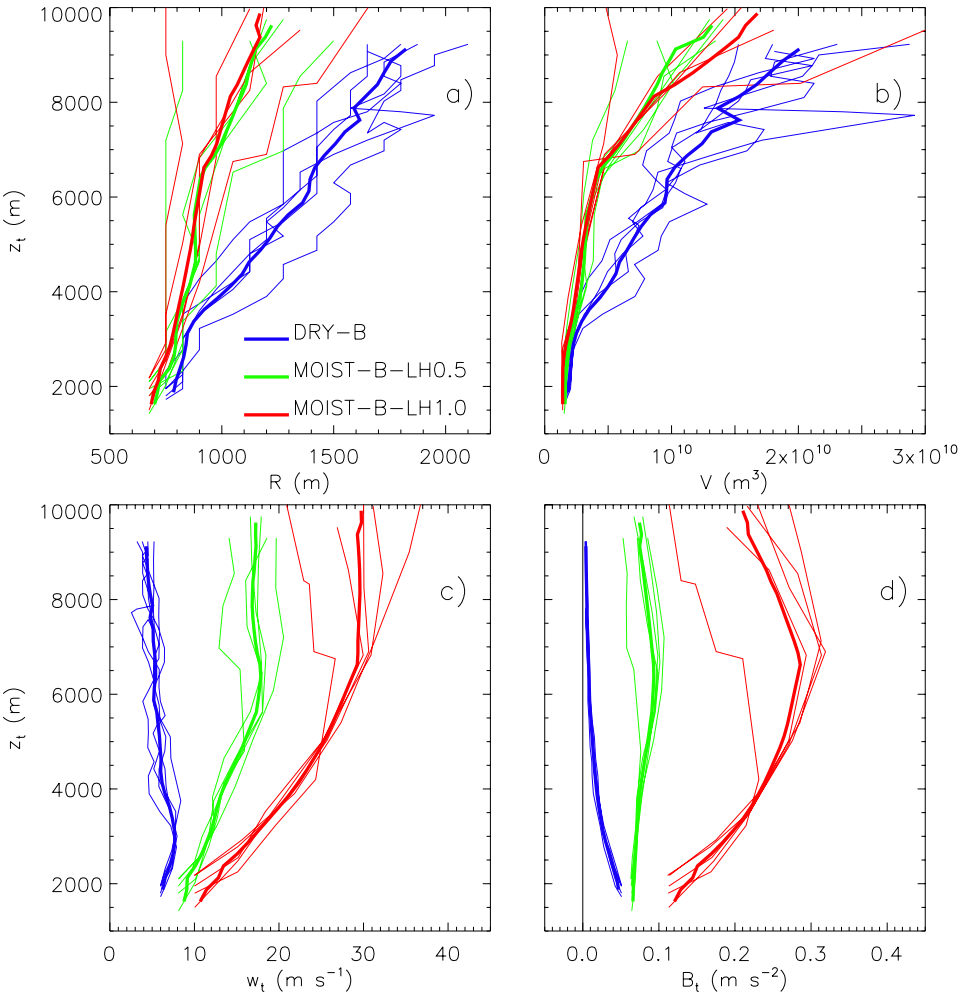

FIG. 3. Various thermal properties as a function of rising thermal top height z_t: a) radius R, b) volume V, c) volume-averaged vertical velocity w_t, and d) volume-averaged buoyancy B_t. Results for the DRY-B (blue), MOIST-B-LH0.5 (green), and MOIST-B-LH1.0 (red) ensembles are presented. Individual ensemble members are shown by thin lines, and ensemble means by thick lines. The thin black vertical line in d) shows the zero line for reference.

One might speculate that the large differences in magnitudes of B_t and w_t between the moist and dry thermals, and their variations with height (i.e., decrease for the dry thermals, but steady or increasing for moist), could have a strong impact on α. This is tested by an additional ensemble using the DRY-B configuration but with the initial bubble θ perturbation increased from 2 to 6 K. This ensemble gives larger B_t by a factor of ~3 and larger w_t by a factor of $\sim 3^{1/2}$ compared to DRY-B, as expected, but almost the same ensemble mean α (0.143 for DRY-B versus 0.153 with

the 6 K bubble). Applying Welch's t-test (accounting for unequal variances of the two samples), these differences are not statistically significant (at 95% confidence) given the ensemble spread. Similarly, another ensemble is tested as in DRY-B except the B field is multiplied by 1.006 at each time step. This increases the buoyancy magnitude over time but has little impact on the spatial distribution of the buoyancy field. The thermals in these simulations indeed have much larger values of B_t and w_t (e.g., 9-12 m/s, and fairly steady or increasing somewhat with height similar to the MOIST-LH0.5 thermals) compared to the main DRY-B ensemble, but values of α (0.209) that are somewhat *larger* than the baseline DRY-B ensemble. Overall, the results from these additional ensembles support the idea that it is the spatial distribution of buoyancy rather than the buoyancy magnitude that is the key factor explaining differences in α between the moist and dry thermals.

b. Verification of the theory for the Boussinesq case

The Boussinesq simulations (DRY-B, MOIST-B-LH0.5, MOIST-B-LH1.0) are next analyzed in the context of the theory presented in section 2. Figure 4 shows the 5 dimensionless parameters in the theoretical expression for α (eq 8) – σ, b, c, f, and ζ, as well as h (thermal aspect ratio) – as a function of thermal top height z_t. Results are presented for ensemble members individually as well as ensemble means. Once the thermals' circulations are spun up, which occurs at z_t ~3 km, all of the parameters are fairly steady with height, except h for the moist thermals which decreases by a factor of about 3 between 3 and 9 km. However, there are some small deviations; for example, f decreases by about 30% between 4 and 9 km for DRY-B, whereas b increases by about a factor of 2 between 6 and 9 km for MOIST-B-LH0.5 and MOIST-B-LH1.0.

Importantly, all of the parameters except σ and h are similar between the moist and dry thermals. This suggests a universal flow behavior of dry and moist thermal flows, which likely reflects their overall similar dynamical structure consisting of ring-like vortices. Again, there are some deviations from the overall similarity of parameter values. Namely, f is up to ~50% smaller above 6 km for the dry compared to moist thermals, while conversely b is larger by a similar magnitude for the moist thermals than dry above 6 km. Because the theoretical α depends on the ratio f/b, these differences mostly cancel. Thus, for the Boussinesq case (in which h is not relevant), the primary difference between the moist and dry thermals is parameter σ – the ratio of buoyancy averaged along the thermal's vertical axis to the thermal-average buoyancy. In the moist thermals,

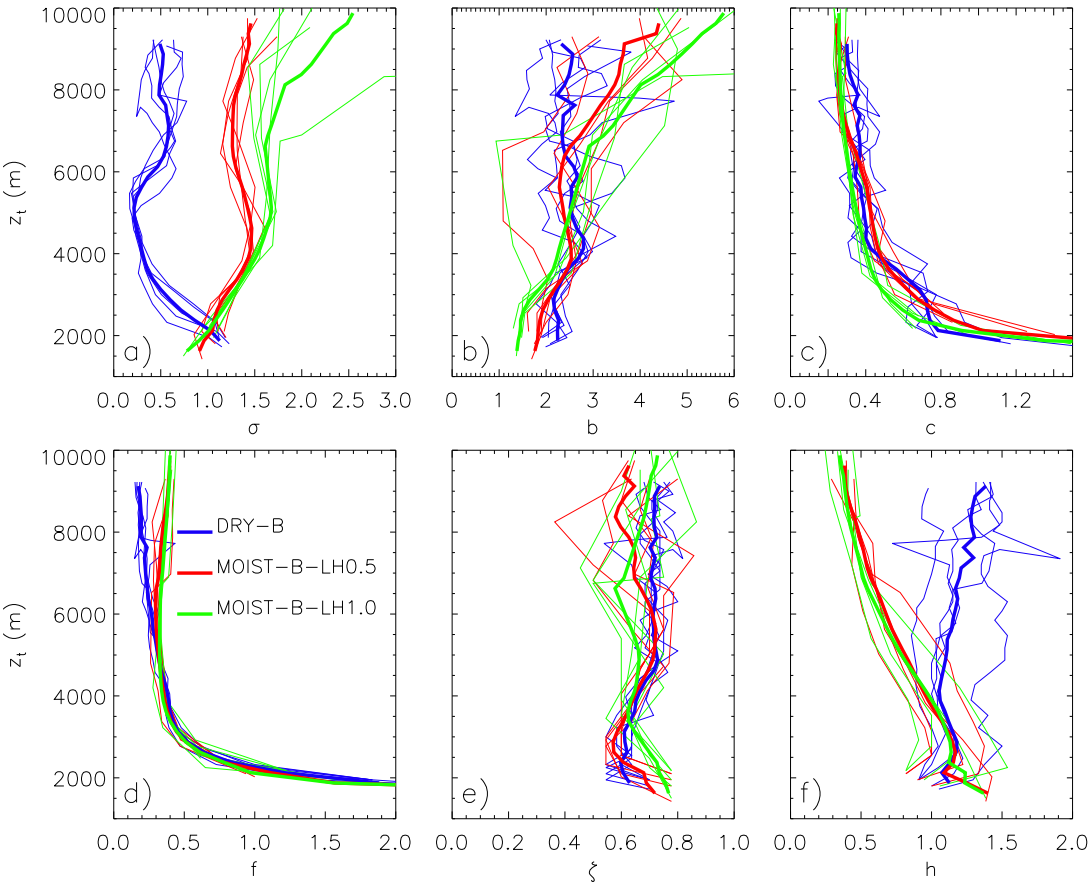

499 FIG. 4. Dimensionless parameters in eqs. (8) and (10) obtained from the simulations as a function of rising
500 thermal top height z_t: a) buoyancy spatial distribution σ, b) circulation b, c) inverse Froude number c, d)
501 $f \equiv H/z_t$, e) ratio of core to thermal radius ζ, and f) thermal aspect ratio h. Results for the DRY-B (blue),
502 MOIST-B-LH0.5 (green), and MOIST-B-LH1.0 (red) ensembles are presented. Individual ensemble members
503 are shown by thin lines, and ensemble means by thick lines.

513 with considerable latent heating in their cores, values of σ are relatively large and mainly between
514 1.2 and 2. In contrast, with no sources or sinks of buoyancy in DRY-B, buoyancy is swept out of
515 the thermals' cores by entrainment and σ drops to small values (~0.1-0.6) after spinup (above ~3
516 km). Note that buoyancy is not entirely removed along the vertical axis of the dry thermals because
517 the flow within the thermals is turbulent, unlike the laminar thermals in LJ2019 and Morrison et al.
518 (2022a, 2023), in which buoyancy was almost entirely removed from the thermals' cores. Overall,
519 parameter values are similar between MOIST-B-LH0.5 and MOIST-B-LH1.0 with overlapping
520 ensemble spreads, although σ tends to be slightly larger for MOIST-B-LH1.0.

Theoretical α are calculated from (8) using values of the nondimensional parameters from each member of the DRY-B, MOIST-B-LH0.5, and MOIST-B-LH1.0 ensembles averaged over z_t from 3 to 9 km; the ensemble means and standard deviations are presented in Table 2. These results are compared to the ensemble means and standard deviations of α directly calculated from the tracked thermals in the simulations. Overall, the theoretical and simulated α values compare reasonably well. In particular, both the theoretical and simulated α values for DRY-B are much larger than those for the moist thermals. Again applying Welch's t-test, both the theoretical and directly simulated α values are significantly different between the DRY-B and the MOIST-LH-0.5 and MOIST-LH-1.0 thermals at greater than 95% confidence level. In contrast, α is not statistically different between the MOIST-LH-0.5 and MOIST-LH-1.0 ensembles. Although the theoretical and simulated α values are very close for DRY-B, the theoretical values are somewhat smaller than simulated for the moist thermals by 0.02-0.05. Reasons for this difference between the theory and simulations are unclear, but may be related to deviations from assumptions invoked in deriving the theoretical α, such as the thermals being spheroidal. That said, given the fairly large spreads for the MOIST-B-LH0.5 and MOIST-B-LH1.0 ensembles, the differences between the theoretical and simulated values are not statistically significant and therefore may not be robust.

Given that σ is markedly different between the moist and dry thermals while the other parameters (except h) are similar, these results further suggest that differences in the spatial distribution of buoyancy are the primary driver of differences in α. This is consistent with MPS21, who showed that adding heating in a narrow core of dry thermals led to a decrease in α. Horizontal gradients of buoyancy ($\partial B/\partial r$) lead to baroclinic generation of vorticity. In the moist thermals, the largest buoyancies are located along the vertical axis (Fig. 2d-f), corresponding to $\sigma > 1.2$, with $\partial B/\partial r$ mostly negative which leads to a vorticity source (positive) throughout the thermal. This increases vorticity throughout the thermal and thus increases circulation, but has a limited impact on the location of maximum vorticity corresponding to the ring vortex radius. Thus, spreading of the ring vortex and the thermal as a whole outward is limited. In contrast, buoyancy is mainly concentrated along the vortex ring (center of rotation) for the dry thermals (Fig. 2a-c), corresponding to $\sigma < 0.6$, with $\partial B/\partial r < 0$ on the outside edge of the vortex ring but $\partial B/\partial r > 0$ on the inner edge. This leads to positive vorticity generation along the outer edge of the ring, but a negative tendency along the inner edge. In effect, this causes an outward migration of the region of largest vorticity

corresponding with the ring vortex, and hence expansion of the thermal, a mechanism previously detailed by Zhao et al. (2013) and McKim et al. (2020) for dry thermals.

TABLE 2. Values of thermal spreading rate α calculated directly from the simulations and from eqs. (8) and (10) using values of the dimensionless parameters from each simulation. α values are averaged over thermal top height z_t between 3 km and the maximum z_t reached by each thermal (9-10 km). Ensemble means ± one standard deviation are presented.

Ensemble	Simulated α	Theoretical α
DRY-B	0.143 ± 0.021	0.140 ± 0.018
DRY-C	0.234 ± 0.048	0.254 ± 0.041
MOIST-B-LH0.5	0.058 ± 0.034	0.042 ± 0.040
MOIST-B-LH1.0	0.063 ± 0.044	0.017 ± 0.052
MOIST-C-LH0.5	0.061 ± 0.029	0.089 ± 0.043
MOIST-C-LH1.0	0.060 ± 0.027	0.106 ± 0.042

c. Impacts of density stratification

We next examine the simulations that include density stratification with compressible dynamics and the dry-neutral environment (the DRY-C, MOIST-C-LH0.5, MOIST-C-LH1.0 ensembles). Results are compared to the theoretical expression for α that includes density stratification (eq 10) with values of parameters σ, b, c, f, ζ, and h from the simulations. Overall, moist and dry thermal structures in the density-stratified environment are similar to those in the Boussinesq simulations. Most important, there are large differences in thermal spreading between the moist and dry cases, and similar differences in buoyancy structure between the moist and dry thermals as in the Boussinesq simulations. Profiles of R, V, w_t, and B_t as a function of z_t for the DRY-C, MOIST-C-LH0.5, and MOIST-C-LH1.0 ensembles with density stratification are shown in Fig. 5. Results from individual ensemble members and ensemble means are presented, along with means from the Boussinesq ensembles for comparison (DRY-B, MOIST-B-LH0.5, MOIST-B-LH1.0). Greater expansion of DRY-C thermals compared to MOIST-C-LH0.5 and MOIST-C-LH1.0 is clearly seen by the profiles of R and V (Figs. 5a,b). Overall, there is little impact of density stratification on the moist thermals except for increased B_t and w_t mainly for MOIST-C-LH1.0. In contrast, thermal

spreading is considerably greater in the density-stratified environment for DRY-C compared to the DRY-B ensemble, but with few differences in w_t and B_t.

Similar to the Boussinesq case, mean α values obtained directly from the density-stratified simulations (Table 2) are different between the moist and dry ensembles at a confidence level greater than 95% using Welch's t-test for both the theoretical and directly simulated values. α for MOIST-C-LH0.5 and MOIST-C-LH1.0 are not statistically significantly different. Theoretical values of α are somewhat greater than the simulated values for both MOIST-C-LH0.5 and MOIST-C-LH1.0, despite being somewhat smaller for the corresponding Boussinesq ensembles. Reasons for these differences are unclear, and again may be related to simplifications and approximations made in deriving the theory; nonetheless, differences in α between the theory and simulations for MOIST-C-LH0.5 and MOIST-C-LH1.0 are within the ensemble spreads.

Profiles of the dimensionless parameters σ, b, c, f, ζ, and h for the density-stratified case are shown in Fig. 6. Parameters values are close to those from the Boussinesq simulations, again suggesting universal behavior of thermal flows. Values are also similar between moist and dry thermals for all parameters, even more than in the Boussinesq simulations, except for σ and h, with ensemble spreads that overlap at almost all heights for DRY-C, MOIST-C-LH0.5, and MOIST-C-LH1.0. Similar to the Boussinesq thermals, the buoyancy distribution parameter σ is quite different between the dry and moist thermals in the density-stratified environment, with DRY-C giving $\sigma < 0.5$ generally after thermal spinup (above ~3 km), and MOIST-C-LH0.5 and MOIST-C-LH1.0 giving σ ~1.2 to 1.6. Important for the density-stratified case, the thermal aspect ratio h decreases with height for the moist thermals, from ~1 at z_t of 3.5 km to ~0.5 at 9 km. In contrast, h slightly *increases* for DRY-C thermals from 1 to ~1.5 across the same height range, although there is considerable scatter among ensemble members.

Profiles of the theoretical and simulated α for the DRY-C, DRY-B, MOIST-C-LH0.5, and MOIST-B-LH0.5 ensembles are shown in Fig. 7a (similar results are obtained for the MOIST-C-LH1.0 and MOIST-B-LH1.0 ensembles as MOIST-C-LH0.5 and MOIST-B-LH0.5). Overall, the theoretical α values are close to the simulated ones for all of the ensembles, and also show similar trends with height[3]. For the density-stratified environment in DRY-C, α increases by more than a factor of 3 for z_t between 3 and 9 km. This trend is well captured by the theoretical α, although the theory

[3]Note the theoretical α values in Fig. 7a use ensemble mean parameter values at each height level, except that the vertically-averaged profile of ζ is used to avoid large fluctuations in α below 3 km (this has little impact on theoretical α values above 3 km).

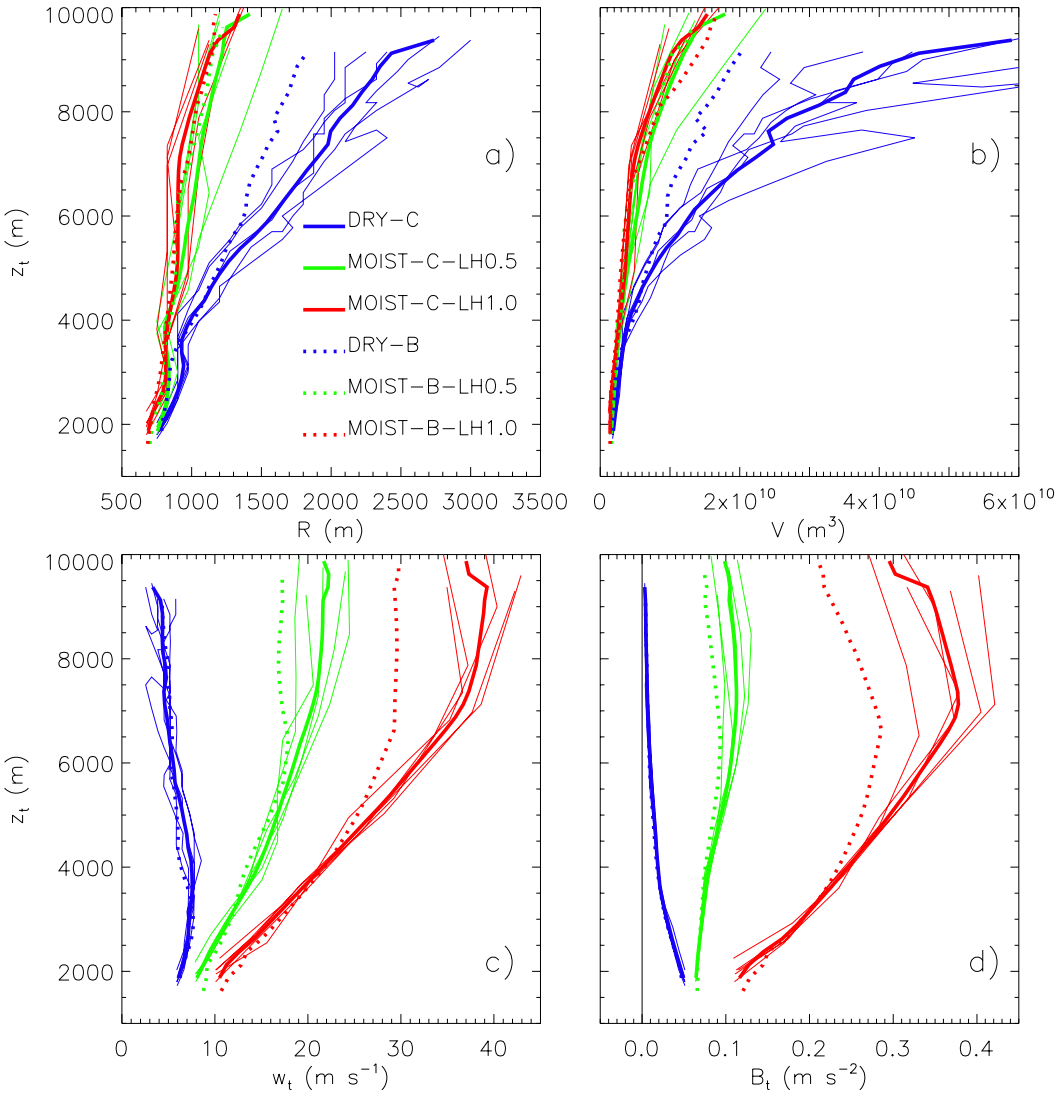

583 FIG. 5. As in Fig. 3 except for the DRY-C (blue), MOIST-C-LH0.5 (green), and MOIST-C-LH1.0 (red)
584 ensembles with compressible dynamics and a density-stratified environment. Also shown by dotted lines are
585 the ensemble means from the Boussinesq DRY-B (blue), MOIST-B-LH0.5 (green), and MOIST-B-LH1.0 (red)
586 ensembles.

607 somewhat underpredicts the simulated values at higher z_t. In contrast, α is fairly constant with
608 height, with even a slight decrease, for the dry Boussinesq case (DRY-B); this slight decrease of
609 α is explained by the small decrease in parameter f with height (see Fig. 6). The slight decrease
610 in f (and hence α) after spinup differs from self-similarity theory, but might be explained by the
611 finite domain size and rigid upper and lower boundaries. Interestingly, the theoretical expression is
612 able to capture the local maximum in α near z_t ~6 km and minimum near 7.5 km from the DRY-C

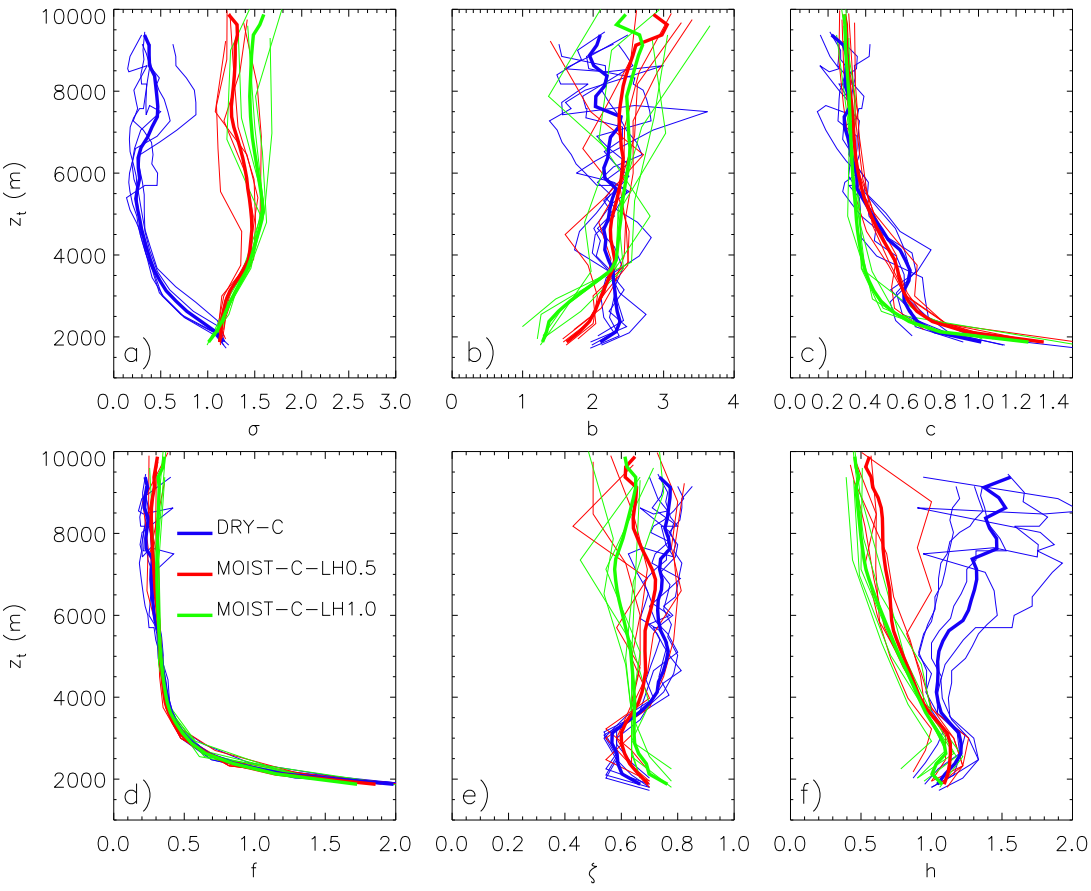

599 FIG. 6. As in Fig. 4 except for the compressible DRY-C (blue), MOIST-C-LH0.5 (green), and MOIST-C-LH1.0
600 (red) ensembles.

613 ensemble. This is a result of variations in σ with height; using a vertically-averaged σ value in the
614 theoretical expression gives a nearly monotonic increase in α with height (not shown).

615 For the moist thermals, the theory shows a small increase in α of ~0.02-0.06 with the density-
616 stratified environment (MOIST-C-LH0.5) compared to the Boussinesq ensemble (MOIST-B-
617 LH0.5), but the increase is much less than that for dry thermals. The simulated α values from
618 MOIST-C-LH0.5 are similar to those from MOIST-B-LH0.5, although α averaged between z_t of 3
619 and 9 km is slightly larger (by 0.02) in MOIST-C-LH0.5 compared to MOIST-B-LH0.5.

626 Figure 7b compares theoretical α values assuming unstratified (eq 8) or density stratified (eq 10)
627 environments using values of the dimensionless parameters from the DRY-C and MOIST-C-LH0.5
628 ensembles. There is a large decrease of α without density stratification for the dry case; moreover,
629 the values do not show any strong trend with height. There is a smaller decrease in α for the moist

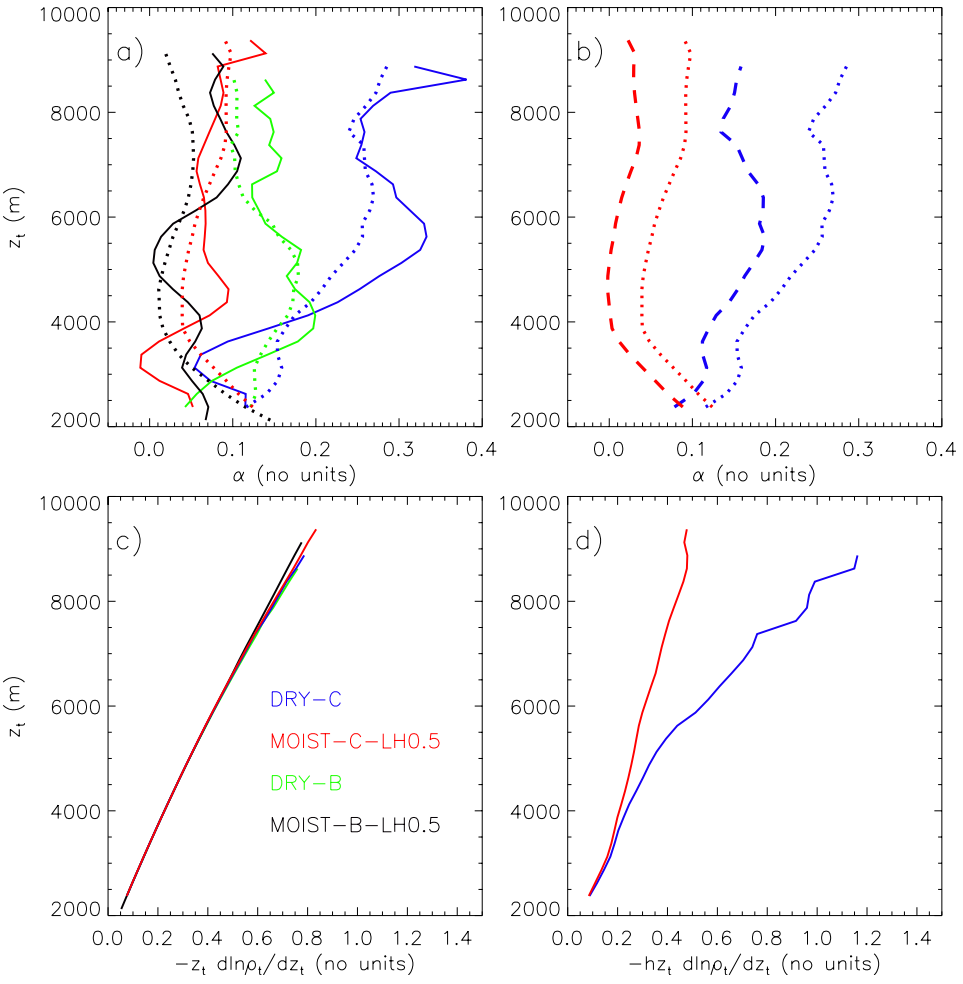

FIG. 7. Profiles as a function of rising thermal top height z_t of: a) theoretical α (dotted lines) using eqs. (8 and 10) with dimensionless parameter values from the simulations and α directly calculated from the simulations (solid lines); b) theoretical α using dimensionless parameters from the DRY-C and MOIST-C-LH0.5 ensembles assuming constant ρ (dashed lines) or with the effects density stratification (dotted lines); c) the density stratification parameter $-z_t d\ln\rho_t/dz_t$; d) density stratification factor including the thermal aspect ratio h ($-hz_t d\ln\rho_t/dz_t$). Colors in all plots correspond to the ensembles as labeled in c).

case without density stratification. These results indicate that density stratification is indeed the reason for the large increase of α with height for the dry case. The stratification factor $-z_t d\rho_t/dz_t$ in (10) increases sharply with height, about an order of magnitude from z_t of 3 to 9 km (Fig. 7c). Since this factor only depends on the air density profile, it is essentially the same for all ensembles (small differences seen in Fig. 7c are a result of discretization and interpolation). Since thermal aspect ratio h is fairly constant with height for the dry thermals, increasing by about 50% but with

a large ensemble spread, this means that the density stratification term in the expression for α, which is equal to h times $-z_t d\rho_t/dz_t$, increases about an order of magnitude at z_t ~9 km (Fig. 7d). This explains the large increase in α when density stratification is considered for dry thermals. In contrast, h decreases by about a factor of 2 with height for the moist thermals. This compensates for the increase in $-z_t d\rho_t/dz_t$, and h times $-z_t d\rho_t/dz_t$ only increases by a factor of 3 for z_t between 3 and 9 km. As a result, the increase in α with height for MOIST-C-LH0.5 owing to density stratification is small compared to DRY-C, and minor vertical variations in the other parameters mask any trends with height.

d. Passive tracer analysis of thermal dilution

Dilution of thermal air is quantified by the reduction of the volume-averaged passive tracer value within the thermal. This is driven by two processes: 1) the expansion of thermal volume and increase in mass associated with net inflow of environmental air (net entrainment); 2) thermal-environment mass exchange via entrainment and detrainment. The first process – dilution by thermal expansion – is quantified by the ratio of initial thermal mass M_i to the total thermal mass M as the thermal top height z_t rises. That is, considering only the net inflow of environmental air into the thermal assuming a tracer value $T_r = 0$, the thermal-averaged tracer would be $\overline{T_r} = T_{r,i} M_i/M$, where $T_{r,i} = 1$ kg kg^{-1} is the initial tracer value in the thermal. In this case, if there was no change in M as the thermal rises, $\overline{T_r}$ would be constant and there would be no dilution by expansion. This is true even though V must increase with z_t in the density-stratified environment to retain constant mass given the decrease of ρ with height (essentially, this holds because the tracer is treated as a mass mixing ratio). The second process – thermal-environment mass exchange – involves detrainment of some mass of thermal air having a T_r value greater than that of the same mass of entrained air. This leads to a decrease in $\overline{T_r}$ with no change in M.

Figure 8a shows $\overline{T_r}$ as a function of thermal top height z_t for the DRY-C, MOIST-C-LH0.5, and MOIST-C-LH1.0 ensembles. Results from individual ensemble members and ensemble means are presented. Also shown in Fig. 8a (dotted lines) are ensemble mean values of the ratio M_i/M to approximate the mean tracer decrease because of thermal spreading. Consistent with larger α and V for the dry compared to moist thermals, M_i/M is much larger for the MOIST-C-LH0.5 and MOIST-C-LH1.0 than DRY-C thermals. Note that MOIST-C-LH0.5 and especially MOIST-C-

LH1.0 have $M_i/M > 1$ because of net detrainment and a decrease in M during thermal spinup at z_t below ~3 km. Thus, increased net mass entrainment associated with greater α for the DRY-C thermals contributes more to dilution than in the MOIST-C-LH0.5 and MOIST-C-LH1.0 thermals. However, despite this difference, overall thermal dilution as quantified by $\overline{T_r}$ is remarkably similar among the dry and moist simulations. In general, the ensemble mean values of $\overline{T_r}$ are within the ensemble spreads, except for slightly reduced dilution in MOIST-C-LH0.5 and MOIST-C-LH1.0 compared to DRY-C above z_t ~6 km (with $\overline{T_r}$ about 0.03-0.05 kg kg^{-1} greater). Thus, there is greater dilution by thermal-environment mass exchange for the moist compared to dry thermals, given their much smaller increase in M (consistent with much smaller α) yet similar mean tracer profiles.

The reduction of thermal tracer by mixing between the thermals and their environment via mass entrainment and detrainment is quantified by a mixing efficiency defined as $\chi = 1 - \overline{T_r} M_i / \left(T_{r,i} M\right)$. Larger values of χ indicate greater dilution of thermal tracer by mixing. $\chi = 0$ would indicate no dilution of tracer by mixing (though $\overline{T_r}$ may still decrease from thermal spreading and mass increase). In the opposite limit, $\chi = 1$ would indicate complete loss of tracer within the thermal from mixing. Values of χ for the individual members and ensemble means for DRY-C, MOIST-C-LH0.5, and MOIST-C-LH1.0 are shown in Fig. 8b. Consistent with the larger gap between $\overline{T_r}$ and M_i/M for MOIST-C-LH0.5 and MOIST-C-LH1.0 compared to DRY-C seen in Fig. 8a, χ is about a factor of 2.5-3 larger for MOIST-C-LH0.5 and MOIST-C-LH1.0 (χ ~0.5-0.8) than DRY-C (χ ~0.1-0.3) above z_t ~5 km. Note that MOIST-B-LH1.0 has somewhat greater χ than MOIST-B-LH0.5 for $z_t > 5$ km (~0.6 versus 0.7) even though there are no consistent differences in net entrainment as well as entrainment and detrainment efficiencies individually between these ensembles. Reasons for the difference in χ are unclear, but could be related to differences in entrained and detrained tracer values between MOIST-B-LH0.5 and MOIST-B-LH1.0.

Based on these results, it is concluded that despite having much smaller thermal spreading rates (i.e., smaller α, V, and M), moist thermals are similarly diluted as dry thermals. This occurs because moist thermals experience greater dilution from mixing compared to dry thermals, which compensates for their relatively small spreading rates and net entrainment.

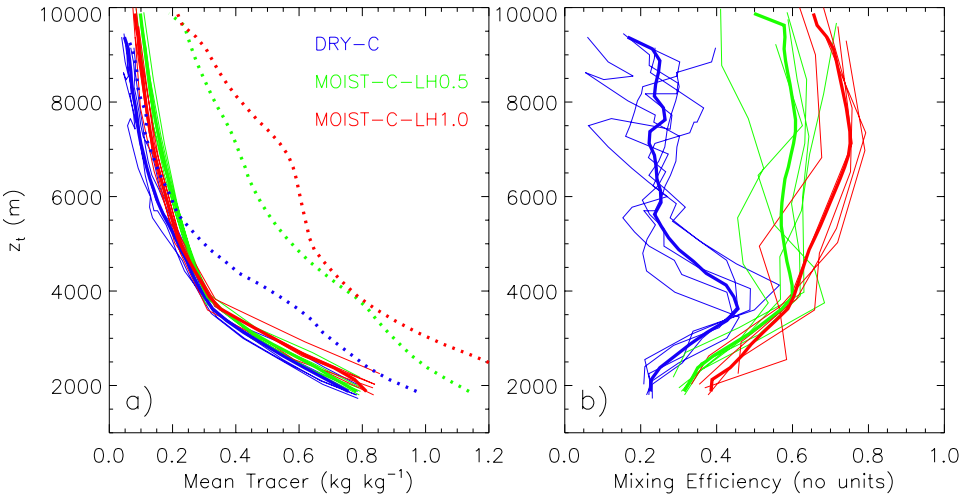

693 FIG. 8. Profiles as a function of rising thermal top height z_t of: a) thermal volume-mean passive tracer $\overline{T_r}$
694 and b) mixing efficiency χ as a function of rising thermal top height z_t for the DRY-C (blue), MOIST-C-LH0.5
695 (green), and MOIST-C-LH1.0 (red) ensembles. Results are presented for the individual ensemble members (thin
696 solid lines) and ensemble means (thick solid lines). Also shown by dotted lines in a) are ensemble mean values
697 of the ratio of initial thermal mass to evolving thermal mass during the simulation, M_i/M.

698 *e. Analysis of entrainment and detrainment*

699 In this section, we examine the mass exchange between thermals and their environment further by
700 analyzing entrainment and detrainment rates obtained from the direct parcel calculation. Results
701 are presented for the DRY-C, MOIST-C-LH0.5, and MOIST-C-LH1.0 ensembles, with overall
702 similar results for the Boussinesq simulations (not shown) except as noted below.

703 Figure 9 shows ensemble mean profiles of total entrainment (E) and detrainment (D), fractional
704 entrainment (ϵ) and detrainment (δ), and entrainment and detrainment efficiencies (e and d,
705 respectively) as a function of thermal top height z_t for the DRY-C, MOIST-C-LH0.5, and MOIST-
706 C-LH1.0 ensembles. Total entrainment E (total mass influx into the thermal per second) is similar
707 among the moist and dry thermals, with E slightly smaller for MOIST-C-LH0.5 than DRY or
708 MOIST-C-LH1.0. Total detrainment (thermal mass outflux per second) is smaller for DRY-C than
709 MOIST-C-LH0.5 and MOIST-C-LH1.0 by a factor of 2-3 above 4 km. E is larger than D in
710 all cases, but the difference between them is larger for DRY-C; thus, net entrainment ($E - D$) is
711 larger for DRY-C than MOIST-C-LH0.5 and MOIST-C-LH1.0. Note that results for DRY-C are
712 noisier for all entrainment/detrainment measures because of the slower ascent rate of thermals in

this ensemble, which leads to more noise in the thermal boundaries determined by the tracking algorithm.

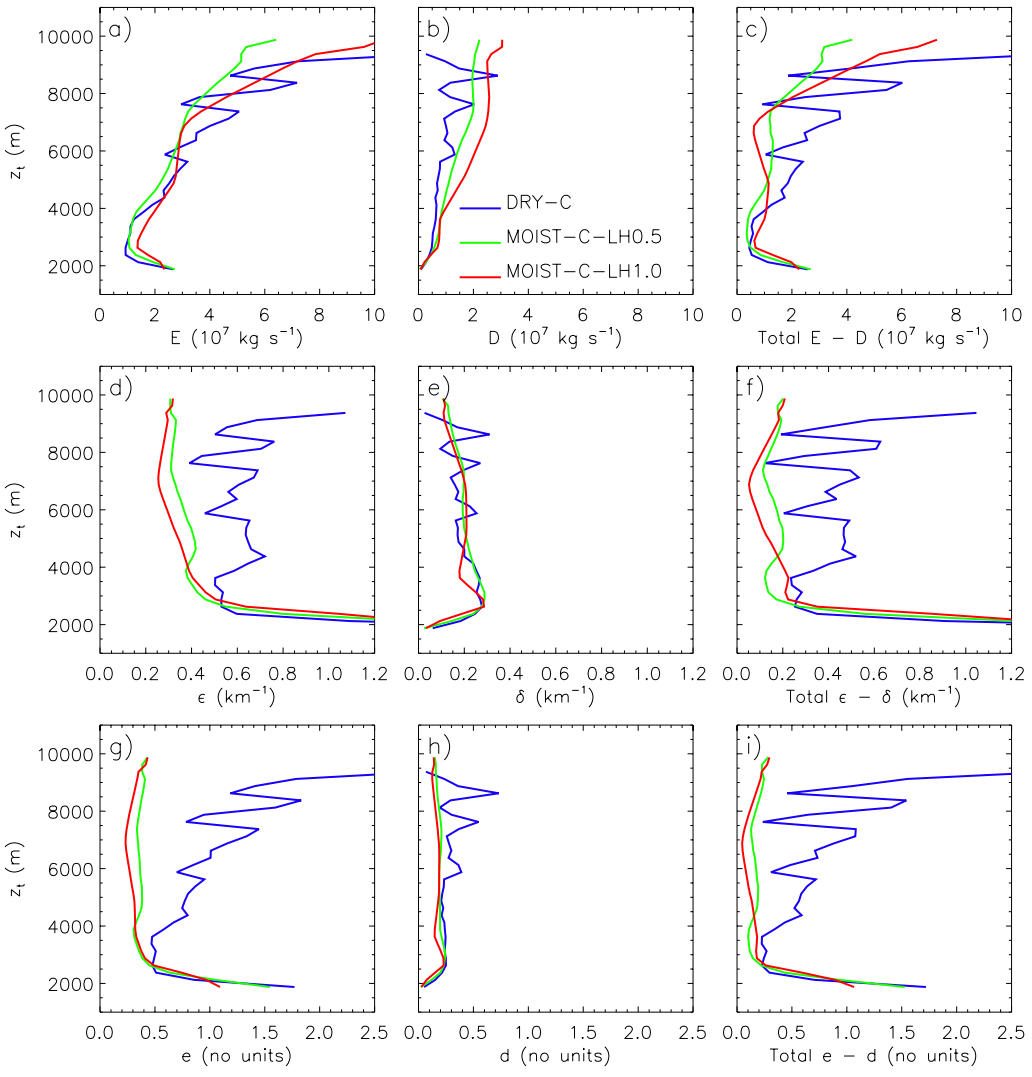

FIG. 9. Profiles of various entrainment and detrainment measures as a function of rising thermal top height z_t: a) total entrainment E, b) total detrainment D, c) total net entrainment $E-D$, d) fraction entrainment ϵ, e) fractional detrainment δ, f) fraction net entrainment $\epsilon-\delta$, g) entrainment efficiency e, h) detrainment efficiency d, and i) net entrainment efficiency $e-d$. Ensemble mean values are shown for the DRY-C, MOIST-C-LH0.5, and MOIST-C-LH1.0 ensembles.

Interestingly, although E is similar among the moist and dry thermals, when it is normalized by the total upward mass transport to give a fractional entrainment rate ϵ, values in the DRY-C ensemble are about a factor of 2-3 larger than in MOIST-C-LH0.5 and MOIST-C-LH1.0. This occurs because

even though the total thermal mass is larger for DRY-C (approximately proportional to thermal volume at a given height z_t), w_t is much smaller and hence the upward mass transport is smaller for DRY-C than MOIST-C-LH0.5 and MOIST-C-LH1.0. Because D is larger for the MOIST-C-LH0.5 and MOIST-C-LH1.0 thermals, when it is normalized by the upward mass transport to give δ, the profiles among DRY-C, MOIST-C-LH0.5, and MOIST-C-LH1.0 are remarkably similar. Consistent with E and D, ϵ is larger than δ leading to positive net fractional entrainment ($\epsilon_{net} = \epsilon - \delta$) for all simulations. However, δ is similar in magnitude to ϵ for the moist thermals, while it is about a factor of 3 smaller for DRY-C. As a result, net fractional entrainment is much smaller for MOIST-C-LH0.5, and MOIST-C-LH1.0 than DRY-C, by about a factor of 3. There are no consistent differences between MOIST-C-LH0.5 and MOIST-C-LH1.0 in terms of fractional entrainment and detrainment.

Multiplying ϵ and δ by R to give non-dimensional entrainment e and detrainment d efficiencies increases differences between the dry and moist thermals compared to ϵ and δ because the dry thermals have larger R. Moreover, because R increases with z_t, e for the DRY-C thermals increases with height and is more than a factor of 5 larger than in MOIST-C-LH0.5 and MOIST-C-LH1.0 above 8 km. ϵ and δ decrease with height by almost a factor of 2 between 3 and 8 km for MOIST-C-LH0.5 and MOIST-C-LH1.0, and when multiplied by R to give e and d, they are nearly constant with height in contrast to the increase for DRY-C. Net entrainment efficiency ($e - d$) is small and fairly constant with height for MOIST-C-LH0.5 and MOIST-C-LH1.0, but is much larger and increases with height for DRY-C. For all of the ensembles, $e - d \approx 3\alpha$, which is the scaling between growth in volume and radius for self-similar thermals (see discussion in the introduction). Thus, even though the shapes of the thermals vary somewhat with height (as evidenced by the aspect ratio h, c.f. Fig. 6), they conform fairly well to this aspect of self similarity. In contrast to DRY-C, the Boussinesq DRY-B thermals give $e - d$ nearly constant with height with a value of $\sim$0.45; this is approximately equal to 3α again consistent with the self-similar scaling.

One benefit of the parcel method for direct calculations of entrainment and detrainment is that the origin location of entrained and detrained parcels can be obtained in a straightforward way. For this analysis, we divide the domain into axisymmetric regions based on height relative to the thermal boundaries and horizontal location relative to the thermal radius. The height intervals are below the thermal bottom, from the thermal bottom to center, from the center to thermal top, and

above the thermal top. The horizontal intervals are radial distance greater than R, from R to $R/2$, and from $R/2$ to the thermal's vertical axis. The four height intervals and three radial intervals give a total of 12 regions (note that the volumes of the regions differ). For every entrained or detrained parcel at each analysis time, when z_t is between 3000 m and the maximum height (between 9000 and 10000 m), the entrained/detrained parcels are assigned to one of the 12 regions based on their location at the previous analysis time (1 min earlier).

The fraction of total entrainment and detrainment events from each of the 12 regions for the DRY-C and MOIST-C-LH0.5 ensembles are shown in Fig. 10 (the MOIST-C-LH1.0 ensemble gives similar results as MOIST-C-LH0.5). The overall pattern of origin location is similar between DRY-C and MOIST-C-LH0.5. Entrained parcels tend to originate along the lateral thermal edge with a majority of parcels originating from below the thermal center (57-63% below and 37-43% above the thermal center), consistent with the idea that entrained environmental fluid in thermals enters through their undersides. In contrast to entrainment, detrainment is strongly favored from the upper half of the thermals, with 73% of detrained parcels in both DRY-C and MOIST-C-LH0.5 originating from above the thermal center. This confirms the assumption of Morrison et al. (2020) that detrainment is favored in the divergent flow in the upper part of thermals. Overall, both DRY-C and MOIST-C-LH0.5 thermals have a similar spatial pattern in the location of entraining and detraining parcels, even though the magnitude of total entrainment (E-D) is smaller for the moist thermals as noted above.

The total fraction of tracer mass below the thermals, following the analysis of LJ2019, shows small values with a maximum of 1.2% at all times considering all of the ensemble means (not shown). This is consistent with the dry simulations of LJ2019, which they argued meant little overall detrainment. How can this be reconciled with the parcel analysis above indicating considerable detrainment from both the moist and dry thermals? As the thermals evolve, the air within them becomes increasingly dilute and hence the same detrained mass will carry less tracer. Detrained parcels also tend to be more dilute than the average thermal parcel at a given time. Furthermore, there is considerable tracer mass detrained from the thermals but remaining in the environment above the thermal bottom. For example, an average of 29, 57, and 67% of the total initial tracer mass resides in the environment above the thermal bottom for z_t between 3 and 9 km in the DRY-C,

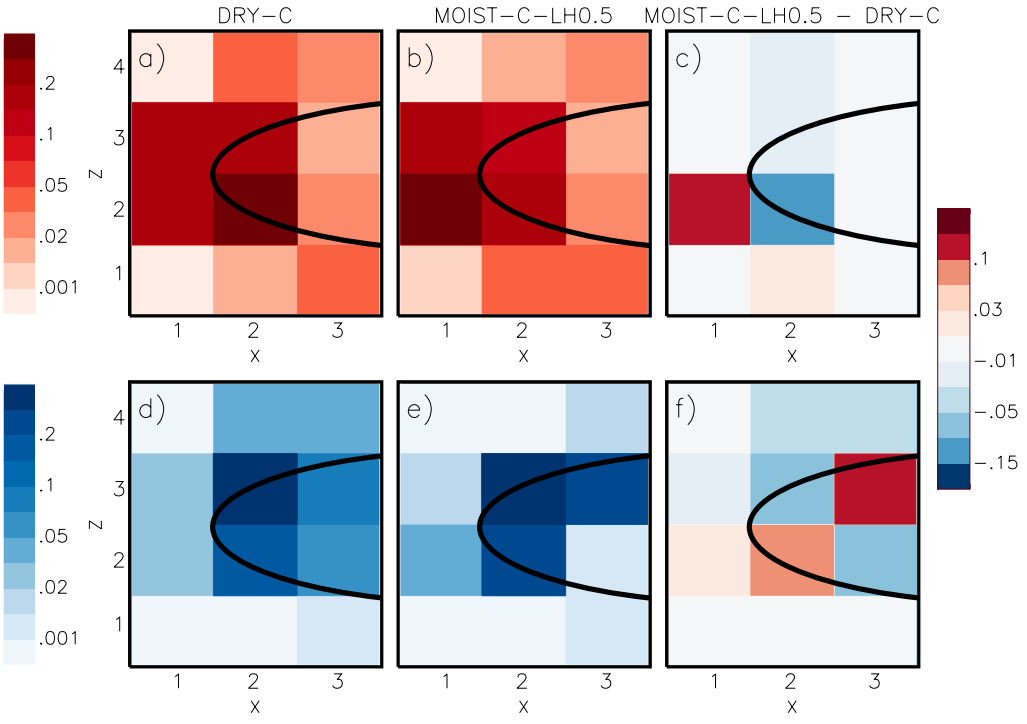

Fig. 10. Origin location of entrained (top panels) and detrained (bottom panels) parcels. Heat maps indicate the fraction of all entrained and detrained parcels originating from each 12 regions that are defined relative to the thermal boundaries (see text for how the origin location is calculated). Numbers along the x-axis indicate horizontal origin location r relative to the thermal's vertical axis at $r = 0$ and radius R. "1", "2", and "3" indicate $r > R$, $R \geq r > R/2$, and $R/2 \geq r < 0$, respectively. Numbers along the y-axis indicate vertical origin location z relative to the thermal bottom z_b, top z_t, and center $z_c = (z_b + z_t)/2$. "1", "2", "3", and "4" indicate $z < z_b$, $z_b \geq z > z_c$, $z_c \geq z < z_t$, and $z \geq z_t$, respectively. For ease of identifying these regions, approximate thermal boundaries relative to these locations are shown by the black curved lines; note that the actual thermal shape differs from these lines. Results are shown for the a, d) DRY-C and b, e) MOIST-C-LH-0.5 ensembles; c, f) show the difference between these ensembles (DRY-C - MOIST-C-LH0.5).

MOIST-C-LH0.5, and MOIST-C-LH1.0 ensembles, respectively. Overall, these results indicate considerable detrainment of thermal mass, but with greater detrainment for moist thermals.

f. Moist thermals in a stably stratified environment

The impacts of stable stratification on moist thermal entrainment, detrainment, and dilution are investigated by analyzing the WK simulations. Vertical cross-sections of buoyancy, vertical velocity, and thermal boundaries at three different times for members of the WK-RH0.425 and

WK-RH0.85 ensembles are displayed in Fig. 11. The moist thermals in this moderately stable (with respect to dry dynamics) environment (Brunt-Vaisala frequency of $\sim 10^{-2}$ s^{-1}) decay as they rise above 5-8 km, at which point they begin to decelerate owing to dilution. While the moist thermals in the dry-neutral environment also undergo dilution, it is much more detrimental to the thermals in the stably stratified WK environment. This leads to reduced B_t and hence w_t, particularly in the drier environment for WK-RH0.425 (42.5% RH) compared to WK-RH0.85 (85% RH). Consequently, the WK-RH0.425 simulation shown in Fig. 11a,c,e becomes dominated by production of negative buoyancy by $t = 10$ min, with only a relatively small region of weakly positive buoyancy above 5 km compared to WK-RH0.85. The development of this negatively buoyant shell around the thermal corresponds to buoyancy reversal caused by mixing of environment and cloud air and evaporation, which has been discussed previously for cumulus clouds (e.g., Grabowski 1993; Strauss et al. 2022) and laboratory thermals (Johari 1992).

Vertical profiles of R, V, w_t, and B_t as a function of thermal top height z_t for individual members and means of the WK-RH0.425 and WK-RH0.85 ensembles (as well as the DRY-C, MOIST-C-LH0.5 and MOIST-C-LH1.0 ensemble means for comparison) are shown in Fig. 12. Above 5-8 km, there is a sharp increase in R and V and decrease in w_t as the thermals begin to decay. This rapid thermal spread occurs because a larger thermal volume is needed to produce a volume-mean velocity (w_t) consistent with the slowing thermal top ascent rate. Inspection of vertical cross sections during this decay process (not shown) suggests the sharp increases in R and V are mainly a feature of the thermal tracking algorithm, as the main dynamical features themselves do not undergo a drastic change (e.g., distance between downdraft maximum near the lateral cloud edge and the cloud center). Below 5-8 km prior to thermal decay, most members of the WK-RH0.425 and WK-RH0.85 ensembles have R and V close to the moist thermals in the dry-neutral environment (MOIST-C-LH0.5 and MOIST-C-LH1.0), but with the WK-RH0.425 thermals having somewhat smaller R and V (and much smaller B_t) for z_t of ~4 to 7 km. Nonetheless, there is one outlier member of the WK-RH0.85 ensemble with much larger R and V compared to the other four members, and it is similar to the dry thermal ensemble mean (DRY-C). In this simulation, a region of strong descent along the upper thermal edge near its horizontal center occurs when z_t reaches ~4 km, with rising turrets on either side. This leads to relatively large buoyancy along the lateral edge compared to the thermal center (and thus small σ, not shown), which favors rapid

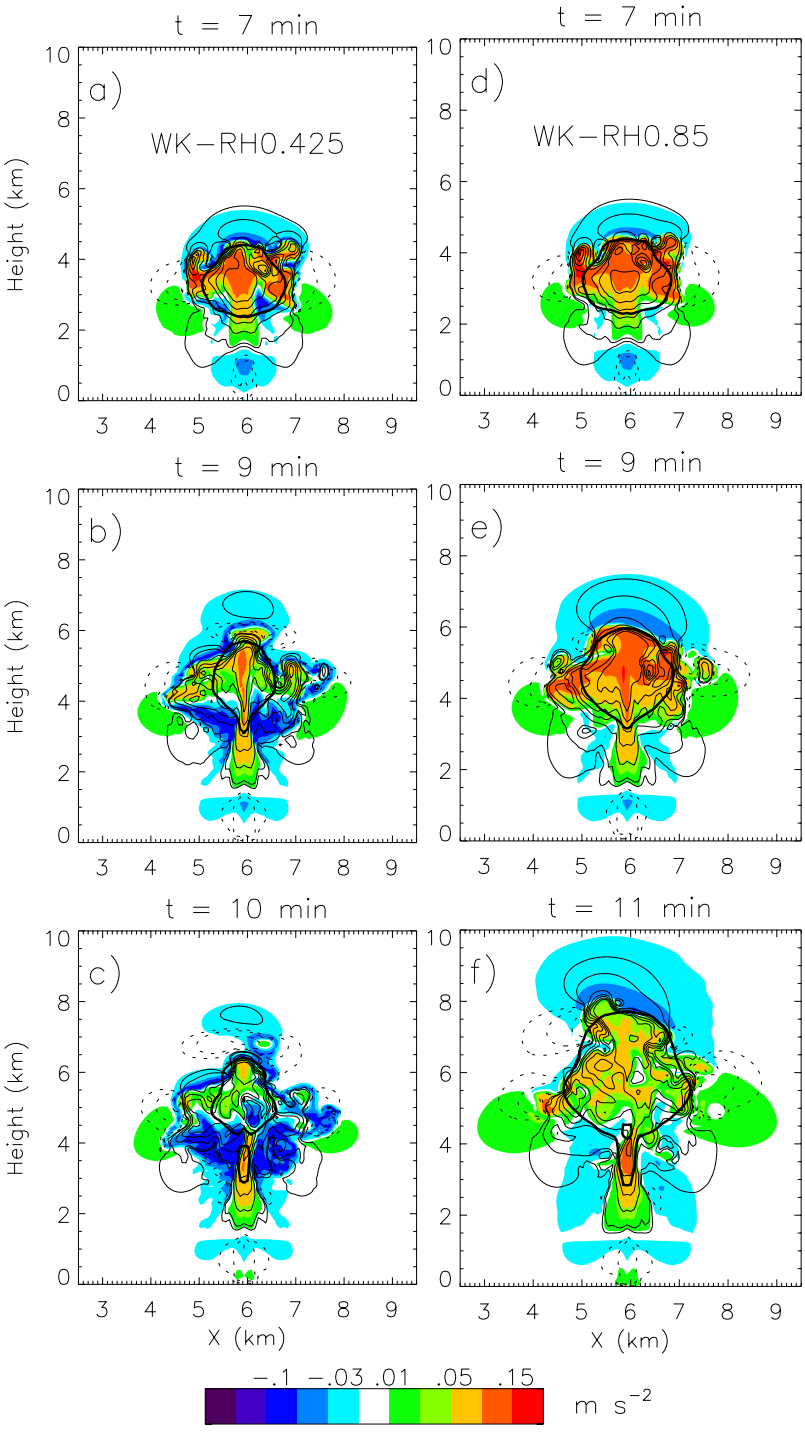

FIG. 11. As in Fig. 2, except members of the a, b, c) WK-RH0.425 and d, e, f) WK-RH0.85 ensembles.

thermal spreading. The thermal in this simulation breaks up into two separate thermals that drift apart horizontally and subsequently decay, which the tracking algorithm interprets as a single large thermal. Note a similar process starts in one member of the WK-RH0.425 ensemble, with relatively

large R and V between about 3 and 4.5 km. However, above that height the thermal undergoes large net detrainment (i.e., negative net entrainment), leading to a sharp decrease in R and V at z_t between 4.5 and 5.5 km.

There are several other notable differences between the moist thermals in the dry-neutral and stably stratified WK environments. Distinct patterns of weakly positive and negative buoyancy occur with forced ascent and descent in the WK environment associated with the generation and propagation of gravity waves (see Fig. 11). In particular, there is a large region of negative buoyancy above the rising thermal top and positive buoyancy in regions of strong descent in the environment along the lateral cloud edge. A key difference between thermals in the WK and dry-neutral environments is greater distortion of the cloud-environment interface for the WK thermals, particularly along the upper thermal edge. This may be driven by the cloud-interface instability discussed in Grabowski et al. (1991). In a stably stratified environment, there is a sharp increase of shear magnitude and decrease of shear layer depth normal to the cloud/thermal interface as it rises. This can lead to the onset of shearing instabilities that grow in amplitude and migrate along the cloud-environment interface. The instability is manifest as smaller-scale (relative to the thermal as a whole) rising, positively buoyant turrets interspersed with negatively-buoyant, penetrative downdrafts, with the latter being favored along cloud top closer to the lateral cloud edges. In contrast, the upper thermal/cloud edge is much smoother in the dry-neutral environment in the MOIST-C-LH0.5 and MOIST-C-LH1.0 ensembles (not shown, but similar to the MOIST-B-LH0.5 cross sections shown in Fig. 2d-f).

Static stability with the WK profile also impacts thermal entrainment and detrainment compared to the dry-neutral environment (Fig. 13). Although total entrainment E is similar among all of the simulations below z_t of 6 km (above which the WK thermals decay and expand rapidly as noted above giving large E), thermals in the WK environment have greater total detrainment D. Detrainment is also generally much greater from the WK-RH0.425 thermals compared to WK-RH0.85, especially at z_t between 4 and 6 km. Physically, this is explained by increased cloud evaporation and buoyancy reversal in the low RH environment in WK-RH0.425, favoring detrainment of cloud regions that mix with the environment. These large mid-troposphere detrainment rates are associated with a breakdown of the broader vortex ring structure. In the example shown in Fig. 11b-c, there is net detrainment from the WK-RH0.425 thermal as it decreases in size and becomes

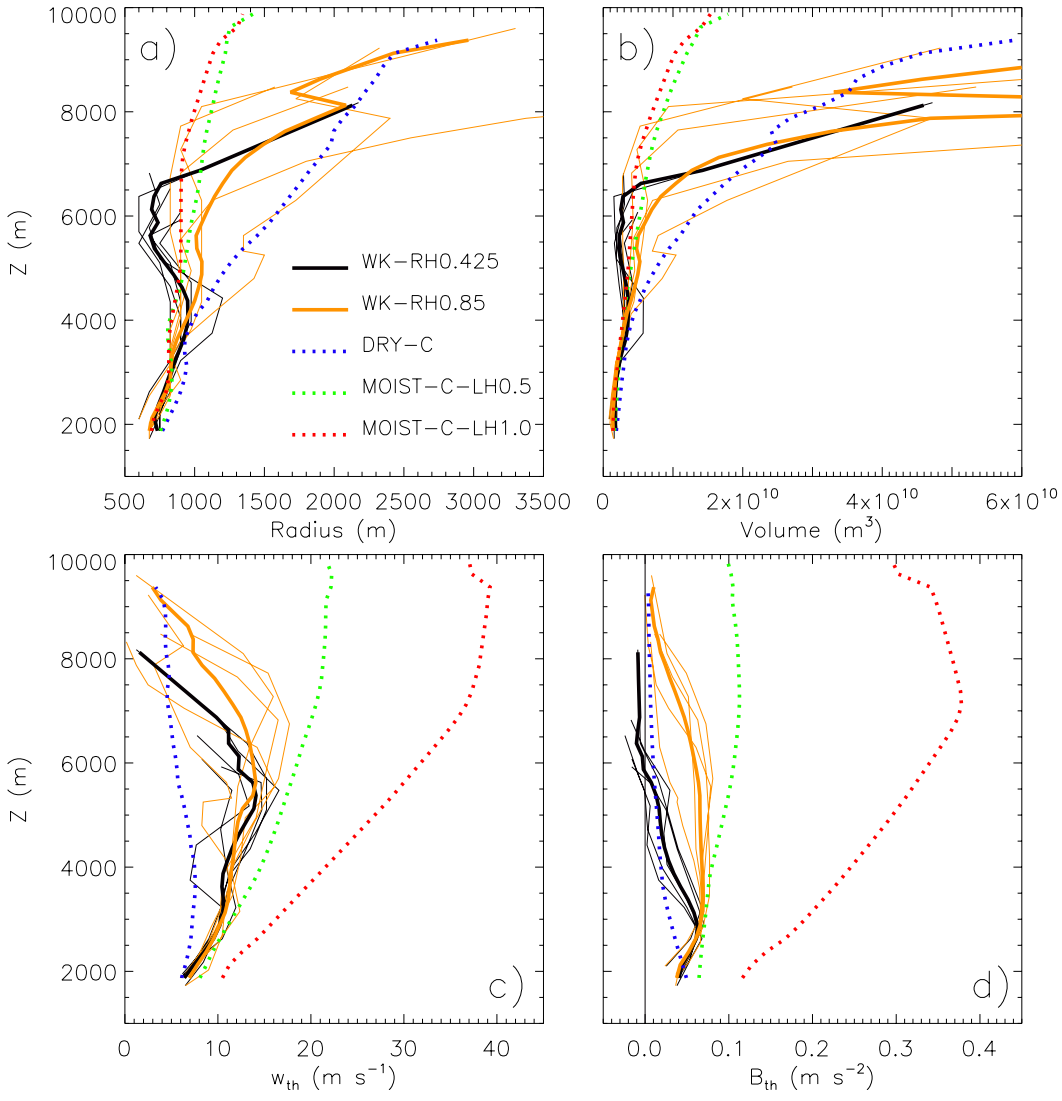

FIG. 12. As in Fig. 3, except for the WK-RH0.425 (black) and WK-RH0.85 (orange) ensembles. For comparison, mean profiles from the DRY-C, MOIST-C-LH0.5, and MOIST-C-LH1.0 ensembles are shown by the dotted lines.

centered on the uppermost rising turret. This sensitivity to RH in the WK environment contrasts with moist thermals in the dry-neutral environment, which are less sensitive to environmental RH at mid-levels. Although there is an increase of δ with reduced environmental RH for the dry-neutral case, the magnitude of this increase is much less than that for the WK environment. Physically, the reduced lapse rate of the WK environment means that cloudy parcels that mix with dry environmental air have a higher likelihood of becoming negatively buoyant and detraining from the updraft thermal than in the dry-neutral case. This is evidenced by the shell of negative buoyancy

surrounding the thermal in the low RH WK case (Fig. 11a-c) that is not seen in the corresponding low RH dry-neutral case (not shown).

Normalizing by the vertical mass flux, fractional entrainment and detrainment rates (ϵ and δ) are greater for WK-RH0.425 and WK-RH0.85 compared to MOIST-C-LH0.5 (with its dry-neutral environment). Similarly, the entrainment and detrainment efficiencies e and d are greater for the WK thermals than MOIST-C-LH0.5. Despite larger entrainment and detrainment rates individually for the WK thermals, there is only slightly greater mixing efficiency χ and similar evolution of the thermal-mean tracer as the dry-neutral thermals (not shown). This suggests the enhanced mixing of thermal and environmental air via entrainment and detrainment in the WK simulations does not have much impact on overall thermal dilution. This may occur, for example, if detrained air tends to have a lower tracer value than the thermal mean. These results are consistent with Johari (1992), who showed that buoyancy reversal strongly influenced the detrainment behavior of laboratory thermals but with limited impact on their overall dilution.

6. Summary and conclusions

In this study, the entrainment, detrainment and dilution behavior of dry and moist thermals was examined via LES. Using an objective thermal tracking algorithm, it was shown that dry thermals have a radius spreading rate ($\alpha \equiv dR/dz_t$) 2.4 times larger than moist thermals in a dry-neutral environment (neutrally stable with respect to dry dynamics) with no density stratification (i.e., applying the Boussinesq approximation). In a dry-neutral, density-stratified environment, α for dry thermals was a factor of 4 greater than that for moist thermals. A theoretical expression for α as a function of several dimensionless flow parameters was derived to provide context for the numerical simulations. Using values of the dimensionless parameters obtained from the simulations, the theory gave similar profiles of α as the simulations for both moist and dry thermals. The parameters were similar among the moist and dry cases, highlighting overall similarity of moist and dry thermal flows, with two critical exceptions: 1) the buoyancy parameter σ, equal to the ratio of buoyancy along the thermal's vertical axis to the thermal-mean buoyancy; 2) the thermal aspect ratio h (radius divided by height). Values of σ were 3-4 times smaller for the dry compared to moist thermals, reflecting buoyancy that was concentrated more in the core of moist thermals and the periphery of dry thermals. The aspect ratio parameter h was larger in the moist compared

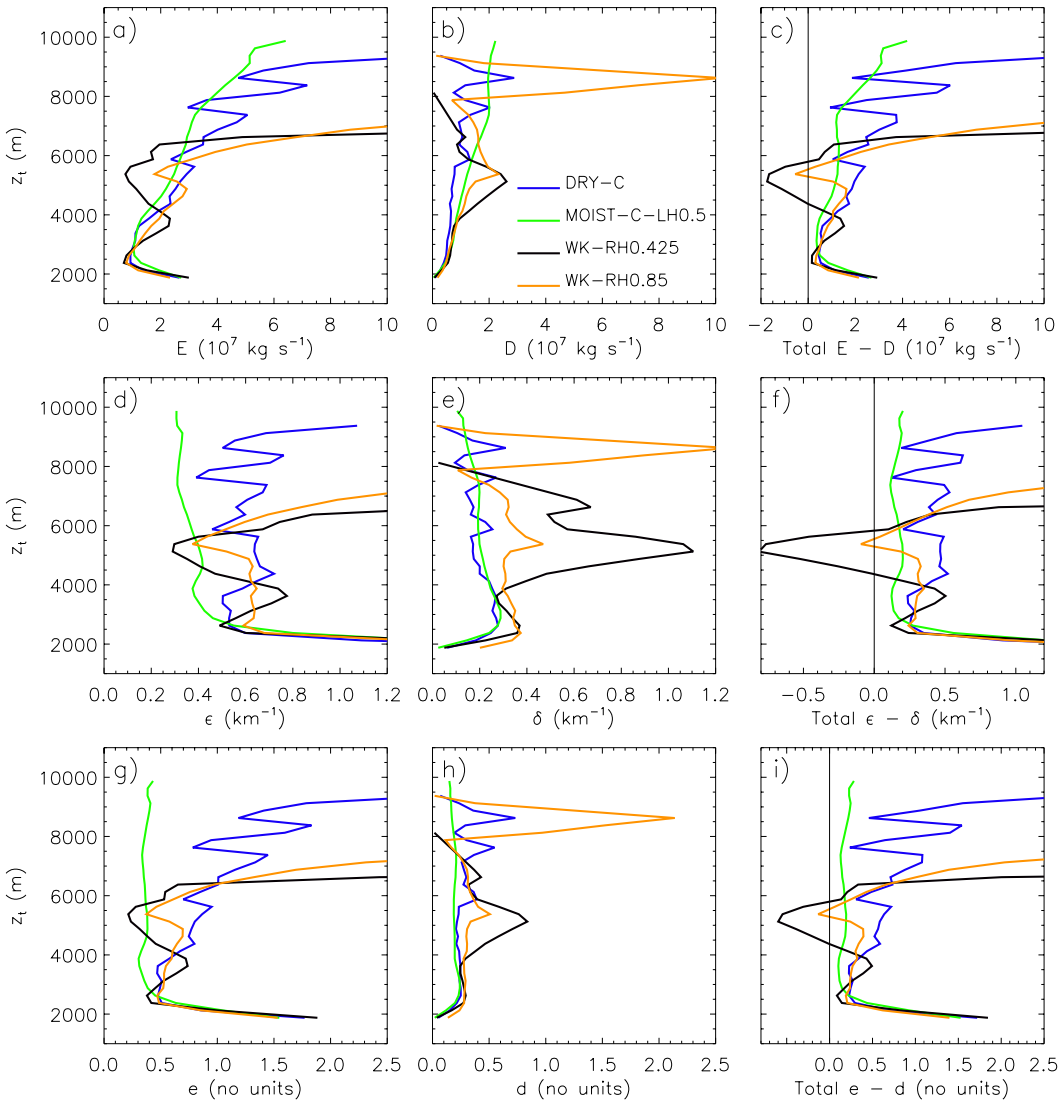

884 FIG. 13. As in Fig. 9, except for the WK-RH0.425 (black), WK-RH0.85 (orange), DRY-C (blue) and
885 MOIST-C-LH0.5 (red) ensembles. The vertical black lines in c), f), and i) indicate zero net entrainment.

902 to dry simulations, and it increased with height for the dry thermals but decreased for the moist
903 thermals. This decrease of h with height for the moist thermals compensated the effects of density
904 stratification, explaining why density stratification had little impact on α for moist thermals. In
905 contrast, the increase in h with height for dry thermals explained the large impact of density
906 stratification on α for dry thermals and the increase of α with height.

907 The smaller α values shown here for moist compared to dry turbulent thermals are qualitatively
908 consistent with the axisymmetric simulations from MPS21. In contrast, VR22 found that spreading

rates were similar between their simulated dry and moist laminar thermals, and somewhat *greater* for moist compared to dry turbulent thermals. The spatial distribution of buoyancy was found to play a key role here, encapsulated by the parameter σ, and the distribution of buoyancy was quite different between the current moist simulations and those of VR22, particularly for their laminar moist thermals. Reasons for these differences are unclear, but might reflect different treatments of the moist thermodynamics (e.g., saturation vapor pressure) and the initial conditions or environmental profiles. Here, condensation began almost immediately for the moist thermals since they were initialized just below the lifting condensation level. This produced a sharp increase of thermal vertical velocity as the thermals rose (e.g., Fig. 3c), whereas VR22 showed a small decrease of vertical velocity in their moist simulations below a height of ~10 radii and an increase only above this height (10 radii here is equivalent to a height of 8250 m). Also note that here thermal height was defined by the thermal top, whereas VR22 defined thermal height based on a vertical velocity centroid. This could also impact the analysis of α, particularly for moist thermals in which the core of higher vertical velocity tends to elongate vertically (Fig. 2f), potentially lowering the centroid height relative to the thermal top.

A direct parcel-based entrainment/detrainment approach was used to examine the behavior of entrainment and detrainment rates individually. In contrast to LJ2019, who found detrainment to be negligible, fractional detrainment rates were comparable in magnitude to fractional entrainment rates. This difference is because LJ2019 calculated detrainment based on the total mass of buoyancy (acting as a passive tracer in their dry simulations) below the thermal, whereas here it was quantified by the total mass of air parcels that were located previously inside the thermal but subsequently moved outside of it. Applying a calculation similar to LJ2019, only ~1% of the tracer mass ended up below the thermals consistent with LJ2019. The direct parcel-based calculation led to much higher detrainment rates because detrained parcels contained a mixture of environmental and initial tracer air, and hence had relatively low tracer values, and because of tracer detrained into the environment but remaining above the height of thermal bottom. Fractional entrainment and detrainment rates were similar in magnitude for moist thermals, while fractional detrainment was relatively small compared to entrainment for dry thermals. This indicates relatively greater thermal-environment mixing (rate of mass exchange) for moist compared to dry thermals, which was also shown by VR22. As a result, moist thermals had an increased mixing efficiency and

similar dilution compared to dry thermals as quantified by a thermal-mean passive tracer, despite having smaller *net* entrainment rates (consistent with smaller α). This analysis also showed that a small majority of entrained parcels originated in the environment below the thermal center (~60%), while most detrained parcels (73%) originated from within the upper half of the thermals.

Additional simulations of moist thermals in a stably stratified environment (WK sounding) were compared to those in the dry-neutral environment. Thermal spreading rates were similar between the WK and dry-neutral simulations up to the height where the WK thermals began to decelerate and rapidly decay owing to buoyancy dilution above ~5-8 km. The parcel analysis showed enhanced fractional entrainment and particularly detrainment rates (up to 5 times larger) in the stably stratified simulations. This was attributed in part to a cloud-interface shear instability along the upper thermal edge in the stably stratified WK environment, detailed by Grabowski et al. (1991), that may have driven deformation of the upper thermal edge and enhanced mixing between the thermal and environment. Increased detrainment in the stably stratified environment, particularly in the simulations with a low environmental relative humidity (42.5%), was also driven by cloud evaporation leading to buoyancy reversal and expulsion of mass from the thermals. This also led to a breakdown of the broader vortex ring structure, resulting in a smaller thermal centered on the uppermost rising cloud turret.

Overall, this study highlights differences in the entrainment, detrainment, and dilution behavior between moist versus dry thermals. Results suggest that smaller-scale mixing driven by entraining and detraining eddies, with net entrainment (entrainment minus detrainment) much smaller than the magnitude of entrainment and detrainment rates individually, is the key contributor to dilution of moist thermals. In contrast, organized entrainment (net inflow and large net entrainment) is the main mechanism driving dilution of dry thermals. Fractional entrainment and detrainment rates that are large individually and similar in magnitude to one another for moist thermals, associated with vigorous thermal-environment mixing, help to explain previous LES results showing moist thermals are generally quite dilute yet undergo little expansion in radius and volume as they rise (Hernandez-Deckers and Sherwood 2016; Peters et al. 2020). This is an important result because dilution of buoyancy is a key factor controlling whether or not convective clouds become deep (in environments that support deep convection), and the vertical velocities within them (Derbyshire et al. 2004; Morrison et al. 2022b). It is also consistent with recent LES studies showing substantial

entrainment and detrainment at almost all cloud levels (e.g., Romps 2010; Peters et al. 2020; Savre 2022), in contrast to convection parameterizations that often assume entrainment occurs at all levels but detrainment is limited to near cloud top (see the review of de Rooy et al. 2013).

Future work should explore the impact of other factors on dilution in moist thermals. For example, previous studies have documented the impact of initial thermal shape and width on cloud dilution (Morrison 2017; Peters et al. 2020). In particular, narrow initial thermals are associated with stronger dilution, reflecting a relationship between fractional entrainment rates and inverse cloud radius (Peters et al. 2020) or area (Rousseau-Rizzi et al. 2017; Mulholland et al. 2021). For simplicity, the thermals in this study were generated by initially motionless, buoyant bubbles added just below the level of free convection. It would be useful to explore thermal entrainment, detrainment and dilution further using a less idealized model setup in which cumulus convection originates from eddies within a turbulent atmospheric boundary layer, and with additional microphysical processes considered including rain and ice initiation.

Acknowledgments. This work was supported by the U.S. Department of Energy Atmospheric System Research grant DE-SC0022942. The NSF National Center for Atmospheric Research is sponsored by the National Science Foundation. High-performance computing support from Cheyenne (doi:10.5065/D6RX99HX) was provided by NSF NCAR's Computational and Information Systems Laboratory. Dr. George Bryan is thanked for developing and maintaining CM1. Dr. Wojciech Grabowski is thanked for providing comments on an earlier version of the manuscript.

Data availability statement. This study used CM1 version 20.1 (cm1r20.1) released on 25 August, 2020. CM1 code and detailed documentation is available at https://www2.mmm.ucar.edu/people/bryan/cm1/. Configuration and namelist files for CM1 simulations as well as analysis code for thermal tracking, calculation of thermal properties, and entrainment/detrainment rates are available at https://doi.org/10.5281/zenodo.13844862, or by request to the author.

APPENDIX A

The impulse-circulation relationship

A useful framework for understanding thermal radius and volume expansion is the constraint provided by momentum conservation (Turner 1957; Lai et al. 2015; McKim et al. 2020; Morrison et al. 2021, 2023). Here it is assumed that the fluid is invsicid and the thermals are axisymmetric in height z and radial r coordinates. The momentum constraint is expressed in terms of thermal circulation Γ, which is defined as the integral of velocity along a circuit ∂S passing through the thermal center along its vertical axis and returning through the ambient fluid. Alternatively, it may be equivalently defined as the area integral of azimuthal vorticity over a region S bounded by the circuit ∂S. This is written as

$$\Gamma = \oint_{\partial S} \mathbf{u} \cdot d\mathbf{l} = \int_S \omega_\phi dr dz \tag{A1}$$

where $\mathbf{u}$ is the flow velocity vector, $d\mathbf{l}$ is a differential length vector in the direction of ∂S, and ω_ϕ is the azimuthal vorticity.

The time rate of change in circulation for an inviscid fluid is

$$\frac{d\Gamma}{dt} = \int_S -\frac{\partial B}{\partial r} dr dz = \int_{z_{bs}}^{z_{ts}} B_c dz \tag{A2}$$

where t is time, $B \equiv -g(\rho - \rho_0)/\rho_0$ is the local buoyancy (g is gravitational acceleration, ρ is local density, and ρ_0 is a background density taken as the horizontal average), B_c is the core buoyancy along the thermal's vertical axis, and z_{bs} and z_{ts} are the bottom and top heights of region S. It is assumed that the region of buoyancy is contained within the thermal, with zero buoyancy in the environment outside of the thermal. This is a realistic assumption for dry, initially spherical thermals (Morrison et al. 2022a). It is also approximately true for moist thermals, although they generally contain some positive buoyancy in their wake and trailing "stem" of convection as shown by the simulations presented in section 5. Equation (A2) shows that the change in circulation is directly related to the thermal's core buoyancy. Positive buoyancy along the thermal's vertical axis leads to an increase in Γ, while negative core buoyancy leads to a decrease.

We can relate thermal radius growth to the thermal top height (z_t) as it rises, $\alpha \equiv dR/dz_t$, via Γ following the impulse-circulation relation. The fluid impulse is defined as the total momentum change starting from rest caused by some external forcing over a finite region of space. In the absence of non-conservative forces and assuming incompressibility, for an idealized, infinite domain the impulse is (Batchelor 2000)

$$I = \frac{\rho}{2} \int_{\mathcal{V}} \mathbf{x} \times \omega d^3 x \tag{A3}$$

where ω is the vorticity vector, $\mathbf{x}$ is a position vector, and $\mathcal{V}$ is the entire domain.

If vorticity is concentrated along a circle of radius R_{vc}, and this region of vorticity is small compared to R_{vc}, which is supported by previous simulations (e.g., MPS21; McKim et al. 2020), then (A3) can be approximated as (Turner 1957; McKim et al. 2020)

$$I_z = \pi \rho_t \Gamma R_{vc}^2 \tag{A4}$$

where ρ_t is the fluid density of the thermal (taken here to be the thermal-averaged ρ). Although 3D turbulent thermals have non-zero vorticity throughout their core, which is augmented by baroclinically-driven eddies in the moist simulations, azimuthal vorticity in the simulations is indeed concentrated within a small region compared to R_{vc}. Following McKim et al. (2020), the subscript "z" is used to indicate that the impulse is only in the z direction as a consequence of axisymmetry of the flow.

To determine the rate of radius growth, we take d/dt of (A4) to give (MPS21, VR22):

$$\frac{dI_z}{dt} = \pi \left(\rho_t R_{vc}^2 \frac{d\Gamma}{dt} + \rho_t \Gamma \frac{dR_{vc}^2}{dt} + \Gamma R_{vc}^2 \frac{d\rho_t}{dt} \right) = F_B \tag{A5}$$

where F_B is the domain-integrated buoyant forcing which is constant in time in a dry-neutral environment with no sources or sinks such as latent heating. Here the change of ρ_t with time as the thermal rises is retained for general applicability to a density-stratified environment.

Following Morrison et al. (2023), (A5) can be combined with (A2) and directly related to α using $w_t = dz_t/dt$ (change in height following the thermal top with time):

$$\rho_t \zeta^2 R^2 \int_{z_{bs}}^{z_{ts}} B_c dz + 2\rho_t \Gamma \zeta^2 R w_t \alpha + \zeta^2 \Gamma R^2 w_t \frac{d\rho_t}{dz_t} = \frac{F_B}{\pi} \tag{A6}$$

where a dimensionless length parameter $\zeta \equiv R_{vc}/R$ is introduced to relate R_{vc} and R.

During spinup of dry thermals, the first term on the l.h.s. of (A6) is positive owing to the presence of thermal core buoyancy before it is swept out from the thermal by entrainment. This leads to a non-zero circulation. With no buoyancy sources or sinks, after the core buoyancy is swept from the thermal, $B_c \approx 0$ and Γ is approximately constant thereafter for an inviscid fluid. Assuming $\rho_t = \rho_0$ is a constant following the Boussinesq approximation, and with $B_c \approx 0$, (A6) can be expressed as

$$2\rho_0 \Gamma \zeta^2 R w_t \alpha = \frac{F_B}{\pi}. \tag{A7}$$

Since Γ, R, w_t, F_b are all > 0 (ρ_0 and ζ are also > 0), this implies $\alpha > 0$ and hence an outward spread of dry thermals as they rise. Moreover, dimensional analysis and self-similarity theory indicates R scales with z_t, i.e., constant α, meaning that w_t scales with z_t^{-1}. The inverse scaling of w_t with thermal height can also be demonstrated independently via the thermal vertical momentum equation (see Morrison et al. 2023 for details). Since $d\rho_t/dz_t < 0$ in a density-stratified environment, the effects of density stratification via (A6) are to increase α for rising thermals; that is, density stratification in the atmosphere always leads to an increase in thermal spreading and thus greater net entrainment.

APPENDIX B

Higher-resolution sensitivity tests

Four additional small (3 member) ensembles with a 32.5 m isotropic grid spacing (factor of ~2.3 smaller that of the main set of simulations) were analyzed to explore sensitivity to model resolution. The DRY-B, DRY-C, MOIST-B-LH0.5, and MOIST-C-LH0.5 configurations were run. Overall results are close to those of the lower resolution simulations. Profiles of thermal R, V, w_t, and B_t as a function of thermal top height z_t for the high resolution simulations are shown in Fig. B1. Consistent with the main simulations, the vertically-averaged ensemble mean α for the Boussinesq dry case (DRY-B) is about a factor of 2 larger than MOIST-B-LH0.5 (0.15 versus 0.076). The difference in mean α between dry and moist thermals increases substantially with density stratification (0.28 for DRY-C versus 0.072 for MOIST-C-LH0.5) similar to the lower resolution simulations. Overall, these results suggest that the main results are robust to changes in grid resolution.

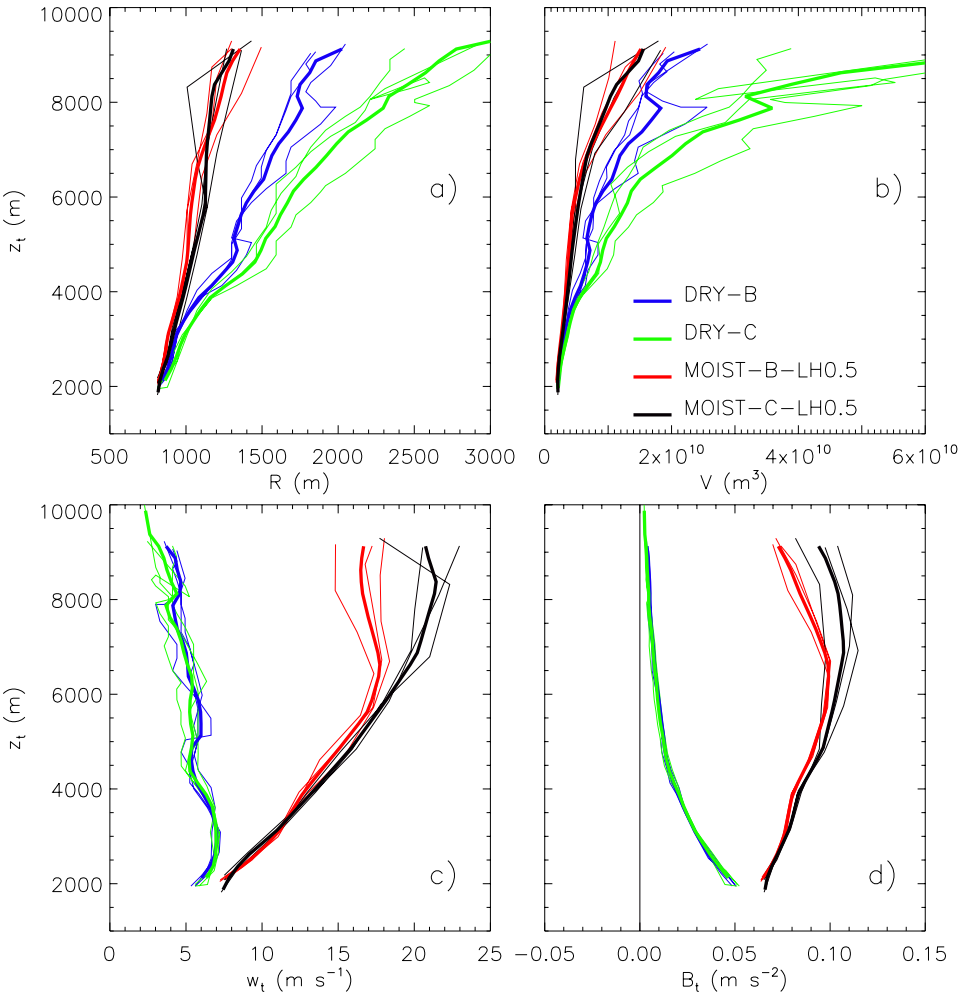

FIG. B1. As in Fig. 3, except for the high-resolution (32.5 m grid spacing) DRY-B (blue), DRY-C (green), MOIST-B-LH0.5 (red), and MOIST-C-LH0.5 (black) ensembles. The vertical black line in d) illustrates zero buoyancy.

APPENDIX C

Symbol	Description
B	Buoyancy
b	Dimensionless circulation parameter defined by $b \equiv \frac{\Gamma}{Rw_t}$

Symbol	Description
B_c	Buoyancy along the thermal's vertical axis
B_t	Thermal volume-averaged buoyancy
c	Dimensionless flow parameter defined by $c \equiv \int_0^{z_t} c_f B_t(z')dz'/(z_t B_t(z_t))$
c_f	Dimensionless scaling parameter defined by $c_f \equiv \frac{1}{2B_t}\frac{dw_t^2}{dz_t}$
D	Total mass detrainment from a thermal to the environment
d	Dimensionless detrainment efficiency
$d\mathbf{l}$	Differential length vector
E	Total mass entrainment from the environment into a thermal
e	Dimensionless entrainment efficiency
e_{net}	Dimensionless net entrainment defined by $e_{net} \equiv e–d$
f	Dimensionless flow parameter defined by $f \equiv H/z_t$
F_B	Volume-integrated buoyant forcing of a thermal
F_e	Vertical momentum entrainment
F_p	Pressure acceleration of a thermal
g	Acceleration of gravity
H	Thermal half depth (vertical depth divided by 2)
h	Thermal aspect ratio defined by $h \equiv R/H$
I	Impulse

Symbol	Description
I_z	Impulse in the z direction (height)
M	Thermal mass
m	Dimensionless thermal shape parameter
M_i	Initial thermal mass
p	Air pressure
q_v	Water vapor mixing ratio
R	Thermal radius
R_{vc}	Radius of vortex core
r	Radial distance
S	Region defined by circuit passing along thermal's vertical axis and returning through the ambient fluid
T	Temperature
t	Time
T_r	Passive tracer
$\overline{T_r}$	Thermal volume-averaged passive tracer
$T_{r,i}$	Initial value of passive tracer within the thermal
$\mathbf{u}$	Fluid velocity vector
u_{axi}	Radial velocity in axisymmetric coordinates
V	Thermal volume

Symbol	Description
W	Ascent rate of thermal top
w	Vertical velocity
w_{axi}	Vertical velocity in axisymmetric coordinates
w_t	Thermal vertical velocity
$\mathbf{x}$	3D position vector
x_c	Horizontal position of thermal center
z	Height
z_b	Height of thermal bottom
z_t	Height of thermal top
z_{ts}	Height of the top of region S
z_{bs}	Height of the bottom of region S
α	Thermal spreading rate defined by $\alpha \equiv dR/dz_t$
Γ	Circulation
δ	Fractional detrainment rate
ϵ	Fractional entrainment rate
ϵ_{net}	Net fractional entrainment defined by $\epsilon_{net} \equiv \epsilon - \delta$
ζ	Dimensionless flow parameter defined by $\zeta \equiv R_{vc}/R$
θ	Potential temperature

Symbol	Description
ρ	Density
ρ_0	Constant background density
ρ_t	Thermal volume-averaged density
σ	Dimensionless buoyancy-related parameter defined by $\sigma \equiv (2HB_t)^{-1}\int_{z_b}^{z_t} B_c dz$
χ	Mixing efficiency defined by $\chi \equiv 1 - \overline{T_r} M_i / M$
ψ	Streamfunction
ω	Vorticity vector
ω_ϕ	Azimuthal vorticity

References

Anders, E. H., D. Lecoanet, and B. P. Brown, 2019: Entropy Rain: Dilution and Compression of Thermals in Stratified Domains. *The Astrophysical Journal*, **884 (1)**, 65, https://doi.org/10.3847/1538-4357/ab3644, URL http://dx.doi.org/10.3847/1538-4357/ab3644, 1906.02342.

Batchelor, G. K., 2000: *An Introduction to Fluid Dynamics*. Cambridge University Press, 615 pp., URL https://books.google.com/books?hl=en{\&}lr={\&}id=7R6FKARyed8C{\&}pgis=1.

Bond, D., and H. Johari, 2010: Impact of buoyancy on vortex ring development in the near field. *Experiments in Fluids*, **48 (5)**, 737–745, https://doi.org/10.1007/s00348-009-0761-z.

Brandenburg, A., 2016: Stellar mixing length theory with entropy rain. *Astrophys. J.*, **832(6)**, 16 pp, doi:10.3847/0004–637X/832/1/6.

Bryan, G., and J. Fritsch, 2002: A benchmark simulation for moist nonhydrostatic numerical models. *Monthly weather review*, **130 (12)**, 2917–2928, https://doi.org/10.1175/1520-0493(2002)1302.0.CO;2.

Damiani, R., G. Vali, and S. Haimov, 2006: The structure of thermals in cumulus from airborne dual-Doppler radar observations. *Journal of the Atmospheric Sciences*, **63 (5)**, 1432–1450, https://doi.org/10.1175/JAS3701.1.

de Rooy, W. C., and Coauthors, 2013: Entrainment and detrainment in cumulus convection: An overview. *Quarterly Journal of the Royal Meteorological Society*, **139 (670)**, 1–19, https://doi.org/10.1002/qj.1959.

Derbyshire, S. H., I. Beau, P. Bechtold, J. Y. Grandpeix, J. M. Piriou, J. L. Redelsperger, and P. M. M. Soares, 2004: Sensitivity of moist convection to environmental humidity. *Quart. J. Roy. Met. Soc.*, **130**, 3055–3079.

Escudier, M. P., and T. Maxworthy, 1973: On the motion of turbulent thermals. *Journal of Fluid Mechanics*, **61 (3)**, 541–552, https://doi.org/10.1017/S0022112073000856, URL http://www.journals.cambridge.org/abstract{_}S0022112073000856.

Grabowski, W. W., 1993: Cumulus entrainment, fine-scale mixing, and buoyancy reversal. *Quarterly Journal of the Royal Meteorological Society*, **119 (513)**, 935–956, https://doi.org/10.1002/qj.49711951305.

Grabowski, W. W., T. L. Clark, W. W. Grabowski, and T. L. Clark, 1991: Cloud–Environment Interface Instability: Rising Thermal Calculations in Two Spatial Dimensions. *Journal of the Atmospheric Sciences*, **48 (4)**, 527–546, https://doi.org/10.1175/1520-0469(1991)048⟨0527:CIIRTC⟩2.0.CO;2, URL http://journals.ametsoc.org/doi/abs/10.1175/1520-0469{\%}281991{\%}29048{\%}3C0527{\%}3ACIIRTC{\%}3E2.0.CO{\%}3B2.

Hernandez-Deckers, D., and S. C. Sherwood, 2016: A numerical investigation of cumulus thermals. *Journal of the Atmospheric Sciences*, **73 (10)**, 4117–4136, https://doi.org/10.1175/JAS-D-15-0385.1.

Jeevanjee, N., and D. M. Romps, 2016: Effective buoyancy at the surface and aloft. *Quarterly Journal of the Royal Meteorological Society*, **142 (January)**, 811–820, https://doi.org/10.1002/qj.2683.

Jiang, G. S., and C. W. Shu, 1996: Efficient implementation of weighted ENO schemes. *Journal of Computational Physics*, **126 (1)**, 202–228, https://doi.org/10.1006/jcph.1996.0130.

Johari, H., 1992: Mixing in Thermals with and without Buoyancy Reversal. *Journal of the Atmospheric Sciences*, **49 (16)**, 1412–1426, https://doi.org/10.1175/1520-0469(1992)049⟨1412:MITWAW⟩2.0.CO;2.

Kirshbaum, D. J., 2020: Numerical simulations of orographic convection across multiple gray zones. *J. Atmos. Sci.*, **77**, 3301–3320.

Kirshbaum, D. J., H. Morrison, and J. M. Peters, 2023: Simplified approximations of direct entrainment and detrainment. *J. Atmos. Sci.*, (submitted).

Kon, H., and C. Magono, 1976: A laboratory experiment of thermals with generation of heat. *J. Meteor. Soc. Japan*, **54(6)**, 427–435.

Lai, A. C. H., B. Zhao, A. W.-K. Law, and E. E. Adams, 2015: A numerical and analytical study of the effect of aspect ratio on the behavior of a round thermal. *Environmental Fluid Mechanics*, **15 (1)**, 85–108, https://doi.org/10.1007/s10652-014-9362-3, URL http://link.springer.com/10.1007/s10652-014-9362-3.

Lecoanet, D., and N. Jeevanjee, 2019: Entrainment in resolved, dry thermals. *Journal of the Atmospheric Sciences*, **76 (12)**, 3785–3801, https://doi.org/10.1175/jas-d-18-0320.1, 1804.09326.

McKim, B., N. Jeevanjee, and D. Lecoanet, 2020: Buoyancy-driven entrainment in dry thermals. *Quarterly Journal of the Royal Meteorological Society*, **146 (726)**, 415–425, https://doi.org/10.1002/qj.3683, 1906.07224.

Morrison, H., 2017: An Analytic Description of the Structure and Evolution of Growing Deep Cumulus Updrafts. *Journal of the Atmospheric Sciences*, **74 (3)**, 809–834, https://doi.org/10.1175/JAS-D-16-0234.1, URL http://journals.ametsoc.org/doi/10.1175/JAS-D-16-0234.1.

Morrison, H., N. Jeevanjee, D. Lecoanet, and J. M. Peters, 2023: What controls the entrainment rate of dry buoyant thermals with varying initial aspect ratio? *J. Atmos. Sci.*, **80**, 2711–2728.

Morrison, H., N. Jeevanjee, and J.-I. Yano, 2022a: Dynamic pressure drag on rising buoyant thermals in a neutrally stable environment. *J. Atmos. Sci.*, **79**, 3045–3063.

Morrison, H., J. M. Peters, K. K. Chandrakar, and S. C. Sherwood, 2022b: Influences of environmental relative humidity and horizontal scale of sub-cloud ascent on deep convective initiation. *J. Atmos. Sci.*, **79**, 337–359.

Morrison, H., J. M. Peters, and S. C. Sherwood, 2021: Comparing growth rates of simulated moist and dry convective thermals. *Journal of the Atmospheric Sciences*, **78 (3)**, 797–816, https://doi.org/10.1175/JAS-D-20-0166.1.

Morrison, H., J. M. Peters, A. C. Varble, W. M. Hannah, and S. E. Giangrande, 2020: Thermal chains and entrainment in moist convection, Part 1: Theoretical description. *J. Atmos. Sci.*, **77**, 3637–3660.

Morrison, H., G. Thompson, and V. Tatarskii, 2009: Impact of cloud microphysics on the development of trailing stratiform precipitation in a simulated squall line: Comparison of one- and two-moment schemes. *Mon. Wea. Rev.*, **137**, 991–1007.

Moser, D. H., and S. Lasher-Trapp, 2017: The Influence of Successive Thermals on Entrainment and Dilution in a Simulated Cumulus Congestus. *Journal of the Atmospheric Sciences*, **74 (2)**, 375–392, https://doi.org/10.1175/JAS-D-16-0144.1, URL http://journals.ametsoc.org/doi/10.1175/JAS-D-16-0144.1.

Mulholland, J. P., J. M. Peters, and H. Morrison, 2021: How does vertical wind shear influence entrainment in squall lines? *J. Atmos. Sci.*, **78**, 1931–1946.

Narasimha, R., S. S. Diwan, S. Duvvuri, K. R. Sreenivas, and G. S. Bhat, 2011: Laboratory simulations show diabatic heating drives cumulus-cloud evolution and entrainment. *Proc. Natl. Acad. Sci.*, **108(39)**, 16 164–16 169.

Peters, J. M., H. Morrison, A. C. Varble, W. M. Hannah, and S. E. Giangrande, 2020: Thermal chains and entrainment in moist convection, Part 2: Analysis of idealized simulations. *J. Atmos. Sci.*, **77**, 3661–3681.

Romps, D. M., 2010: A Direct Measure of Entrainment. *Journal of the Atmospheric Sciences*, **67 (6)**, 1908–1927, https://doi.org/10.1175/2010JAS3371.1.

Romps, D. M., and A. B. Charn, 2015: Sticky thermals: Evidence for a dominant balance between buoyancy and drag in cloud updrafts. *Journal of the Atmospheric Sciences*, **72 (8)**, 2890–2901, https://doi.org/10.1175/JAS-D-15-0042.1, URL http://journals.ametsoc.org/doi/abs/10.1175/JAS-D-15-0042.1.

Rousseau-Rizzi, R., D. J. Kirshbaum, and M. K. Yau, 2017: Initiation of deep convection over an idealized mesoscale convergence line. *J. Atmos. Sci.*, **74**, 835–853.

Savre, J., 2022: What controls local entrainment and detrainment rates in simulated shallow convection? *J. Atmos. Sci.*, **79**, 3065–3082.

Scorer, R. S., 1957: Experiments on convection of isolated masses of buoyant fluid. *Journal of Fluid Mechanics*, **2**, 583–594, https://doi.org/10.1017/S0022112057000397, URL http://www.journals.cambridge.org/abstract{_}S0022112057000397.

Sherwood, S. C., D. Hernández-Deckers, M. Colin, and F. Robinson, 2013: Slippery thermals and the cumulus entrainment paradox. *Journal of the Atmospheric Sciences*, **70 (8)**, 2426–2442, https://doi.org/10.1175/JAS-D-12-0220.1, URL http://journals.ametsoc.org/doi/abs/10.1175/JAS-D-12-0220.1.

Stevens, B., C. H. Moeng, and P. P. Sullivan, 1999: Large-eddy simulations of radiatively driven convection: Sensitivities to the representation of small scales. *Journal of the Atmospheric Sciences*, **56 (23)**, 3963–3984, https://doi.org/10.1175/1520-0469(1999)056⟨3963:LESORD⟩2.0.CO;2.

Strauss, C., D. Ricard, and C. Lac, 2022: Dynamics of the cloud?environment interface and turbulence effects in an les of a growing cumulus congestus. *J. Atmos. Sci.*, **79**, 593–619.

Tarshish, N., N. Jeevanjee, and D. Lecoanet, 2018: Buoyant motion of a turbulent thermal. *Journal of the Atmospheric Sciences*, **75 (9)**, 3233–3244, https://doi.org/10.1175/JAS-D-17-0371.1, URL http://journals.ametsoc.org/doi/10.1175/JAS-D-17-0371.1.

Tian, Y., and Z. Kuang, 2016: Dependence of entrainment in shallow cumulus convection on vertical velocity and distance to cloud edge. *Geophys. Res. Lett.*, **43**, 4056–4065, doi://10.1002/2016GL069 005.

Turner, J. S., 1957: Buoyant Vortex Rings. *Proceedings of the Royal Society A: Mathematical, Physical and Engineering Sciences*, **239 (1216)**, 61–75, https://doi.org/10.1098/rspa.1957.0022, URL http://rspa.royalsocietypublishing.org/cgi/doi/10.1098/rspa.1957.0022.

Turner, J. S., 1963: Model experiments relating to thermals with increasing buoyancy. *Quarterly Journal of the Royal Meteorological Society*, **89 (379)**, 62–74, https://doi.org/10.1002/qj.49708937904.

Vybhav, G. R., and S. Ravichandran, 2022: Entrainment in dry and moist thermals. *Phys. Rev. Fluids*, **7**, 050 501, doi:/10.1103/PhysRevFluids.7.050 501.

Weisman, M. L., and J. B. Klemp, 1982: The dependence of numerically simulated convective storms on vertical wind shear and buoyancy. *Mon. Wea. Rev.*, **110**, 504–520.

Yeo, K., and D. M. Romps, 2013: Measurement of Convective Entrainment Using Lagrangian Particles. *Journal of the Atmospheric Sciences*, **70 (1)**, 266–277, https://doi.org/10.1175/JAS-D-12-0144.1, URL http://journals.ametsoc.org/doi/abs/10.1175/JAS-D-12-0144.1.

Zhao, B., A. W. Law, A. C. Lai, and E. E. Adams, 2013: On the internal vorticity and density structures of miscible thermals. *Journal of Fluid Mechanics*, **722**, 1–12, https://doi.org/10.1017/jfm.2013.158.